Residual Stress Measurement of AISI 304 Stainless Steel Nuclear Canister Plates by X-ray Diffraction

A Major Qualifying Project report to be submitted to the faculty of
WORCESTER POLYTECHNIC INSTITUTE
in partial
fulfillment of the requirements for the Degree of Bachelor of Science

Submitted By

Jessica Ma

Submitted on

April 23rd,2015

Approved by:

Professor Richard Sisson

Abstract

The nuclear fuel storage canisters are used to store spent fuel of the nuclear plants. However, some of the storage sites are located near the sea coast which the environment has high chloride concentration. Such environment along with the residual stress in the AISI 304 stainless steel canister plates caused by welding make them susceptible to stress corrosion cracking. The goal of this project is to study the residual stress in the plates by performing X-ray diffraction method. The macro and micro hardness as well as microstructure of the plates were also measured and examined.

Acknowledgement

I want to thank both of my advisors, Professor Richard Sisson from Worcester Polytechnic Institute, and Professor Ronald Ballinger from Massachusetts Institute of Technology for their advices and support. I really appreciate that I have an opportunity to work on this amazing project.

I would gratefully acknowledge the support of Dr. Boquan Li from Worcester Polytechnic Institute and Mr. Peter Stahle from Massachusetts Institute of Technology on sample preparation and instrument training. I also would like to thank graduate students from WPI, Yuan Lu and Haixuan Yu, for their valuable time and generous support to help me to achieve the goals of this project.

This work was supported by the H.H. Uhlig Corrosion Lab's project of the Life Prediction of Spent Fuel Storage Canister Material, which is funded by U.S. Department of Energy under Award Number: DE-AC07-051D14517

Contents

Table of Figures

Introduction

The spent nuclear fuel is expected to be stored on the fuel rods at the nuclear plants. In service, these rods need to be changed periodically because they tend to lose efficiency over time. When the rods are replaced, the spent fuel that already existed in the rods will be moved to the pools of water at the reactor site where the fuel will be kept safely. The newly generated spent fuel will fill up the new rods in the plants and such process occurs over and over again. In early 1980s, the pools were found having a low capacity and the concept of dry storage cask canisters appeared. [1] A typical storage cask canister has a metal cylinder which contains the spent fuel and such canister is surrounded by a metal or concrete cask to prevent radiation. The cask system is safe and environmentally friendly which it provides heat management, radiation, and nuclear fission containment. Such system also resists earthquake, projectiles, tornadoes, floods, temperature extremes and others natural or human related catastrophes. The spent fuel in the canister only emits a little amount of heat and its heat emission and radioactivity decrease over time. Therefore, the dry cask system provides the maximum safety for nuclear fuel storage. [2]

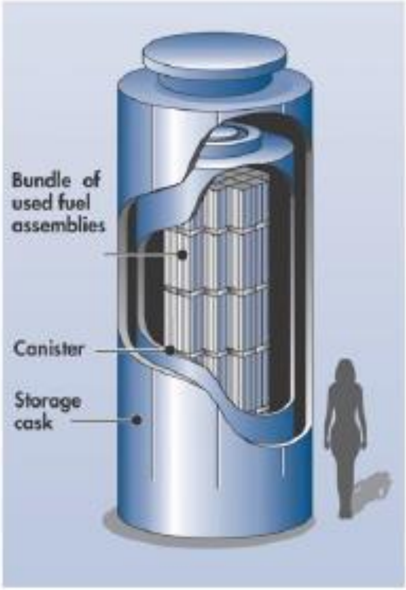

Figure 1. Dry Cask Storage System [3]

The Yucca Mountain is a former site for storing the spent nuclear fuel and it has been shut down in recent in years due to the potential safety issues. The new sites for the keeping dry cask canisters are either near the coast or a lake region. It has been found that the site environment contains Na, Ca, and Mg based salt. This causes serious problem for the canisters which they are susceptible to stress corrosion cracking when exposing to a high chlorine concentration environment. Since the canisters are made of AISI 304 stainless steel plates and the plates are welded together, these canisters have a higher chance of crack failure. [1] The salt containing air contacts with the canisters through venting along with the residual stress remained in the plates due to welding can cause serious stress corrosion cracking in the canisters. The sensitization of the heat affected zone can also cause the local microstructural change. Lastly, the surrounding temperature also plays a role to determine the final susceptibility of the plates. The crack can occur at a temperature of 30 degree Celsius. [4] Theoretically, the predicted service life of the dry cask canisters is around 100 years. However, in recent studies, the stainless steel piping in the nuclear plants suffered from stress corrosion cracking due to salt containing environment which its service life reduced to 30 years compare to 100 years. [1]

Therefore, the goal of this Major Qualifying Project (MQP) is to measure the residual stress within the canister welded plates. The main method used was X-ray diffraction and the strain data obtained will be combined with data acquired from neutron diffraction and contour method to form a database. X-ray diffraction only has a penetration depth around 10 to 50 μm below the surface, while neutron diffraction could provide a penetration depth within the range of 1 to 20 mm and contour method could provide strain information right at the surface, such comprehensive data set will provide accurate stress information within the sample. The stress data set will also be applied in the final probabilistic service life model of the canisters to predict the chance of material failure during the periods up to 100 years with the presence of chlorine contained environment and residual stress.

Background

Residual Stress

Residual stress is considered as “lock-in” stress within the structures without presence of external load. Such stress is typically self-equilibrating which the local tensile and compressive stress cancel each other out and the moment resultants are also zero. Almost all manufacturing processes create residual stress within the sample structures and such stress can also grow as the structures are in service. When these structures serve within their service life, the non-uniform plastic deformation may present which can cause local structural changes such as strain mismatch within the materials. To balance out such changes, some parts within the materials must deform elastically to preserve the integrity of the structure. Thus, such elastic deformation can produce residual stress. [5]

There are three different types of manufacturing processes that can induce residual stress within the structures [5]:

1. Non-uniform plastic deformation caused by forging, rolling, bending, extrusion, and in service surface deformation, etc.
2. Surface modification caused by grinding, machining, peening, and in service corrosion, etc.
3. Material phase and density change caused by welding, casting, quenching, phase transformation, and in service radiation damage in nuclear reactors, etc.

There are also three different types of residual stress [5]:

1. Type I residual stress is macro stress that occurs in a distance range lager than microns.
2. Type II residual stress is micro stress that occurs in a distance range in microns.
3. Type III residual stress is the stress occurs at atomic level near dislocations within the crystal structure and at crystal interfaces.

It has been found that Type I stress may be one cause of Type II stress. In this project, we mainly examined Type II stress which is the stress that occurs in a distance within micron range.

Residual stress can be both beneficial and harmful. Residual stress can be beneficial in the case of the toughened glass. Such glass possesses a high compressive residual stress which helps it to improve its crack resistance. However, in the canister case, the presence of the residual stress can be harmful. Since the residual stress is not distributed evenly within the structure, for example, partially tensile and partially compressive with different magnitudes, the large stress gradients exist, especially in welded samples. The location of the high stress concentration gradient is also uncertain. Therefore, to predict the occurrence of stress corrosion cracking in the structure, it is crucial to make many measurements on small and different parts of the samples to determine the location and magnitude of the largest stress gradient. [5]

Residual Stress Induced by Welding

Welding involves in joining two materials by heating. In the canister case, two stainless steel plates are heated over a high temperature until both edges of the plates melt. Then a filler material will be added to molten metal to join two edges together which the joint becomes the weld centerline. The entire structure then cools down. The heat affected zone refers to the area within the structure that is not being heated during welding but its microstructure has been altered by the heat. The hot molten metal and the heat affected zone cool down over a large temperature range which eventually shrink a lot. To maintain the structural integrity and to response to the strain change due to welding, a longitudinal tensile stress is produced along the weld centerline to balance the compressive stress which causes the structure to contract upon cooling. After the structure cools down completely, the tensile residual stress remains across the centerline which creates compressive stress in the area further away from weld centerline to cancel out the stress. The tensile stress along the weld centerline is proved to reduce material’s fatigue strength and fracture toughness. [5] [6]

AISI Stainless Steel 304

AISI 304 stainless steel has high strength and corrosion resistance. It is mainly composed of chromium, which contributes to its corrosion resistance, and nickel, which mainly contributes to its strength. Its chemical composition can be found in Table 1 below. By using GE USN 60

Ultrasonic Portable Flaw Detector, our group found the velocity of sound in the canister plate sample. Using velocity along with the density and Poisson ratio of the 304 stainless steel, we were able to determine the elastic modulus of the sample. The result and a more detailed measurement process can be found in result and methodology sections.

Chemical Component	C	Mn	P	S	Si	Cr	Ni
304L SS	0.03%	2.0%	0.045%	0.03%	1.0%	18-20%	8-12%

Table 1. Chemical Composition of 304 Stainless Steel [7]

AISI 304 stainless steel has been found to be very vulnerable to stress corrosion cracking under various conditions. In the case where it is being welded, the sensitization of heat affected zone leads it to fail through stress corrosion cracking since the chromium inside, which mainly contributes to the corrosion resistance of stainless steel, depletes at grain boundaries due to precipitation of chromium carbide during welding. This low carbon stainless steel is highly vulnerable to crack. Furthermore, in the chloride containing environment, as the chromium oxide layer breaks, pitting can occur which is followed by the corrosion. In this case, more negative chloride ions flow into the pit to balance positive metal ions which causes corrosion. Corrosion occurs quickly in such high chloride containing, strongly acidic, and nearly saturated solution. Thus, the 304 stainless steel suffers severely from stress corrosion cracking in the canister case where both welding effect and chloride containing environment are present. [4] [6]

However, other studies suggested that 304 stainless steel can also fail due to stress corrosion cracking in the chloride containing environment at ambient temperature without being welded. The surface condition of the stainless steel plays a main role in this case. Surface machining and grinding can aggravate the effect of stress corrosion cracking by increasing surface roughness, inducing surface tensile stress, and enlarging defect density. Machining of AISI 304 stainless steel increases its susceptibility to stress corrosion cracking. It can induce surface plastic strain and deformation which result in the transformation of austenite matrix near the surface into martensite. Such transformation results in a large amount of work-hardening of the material. The work hardened layers cause the material to crack much faster in the chloride solution. Since the canister plates were grinded for surface cleaning once welding was done, the surface deformation by such machining requires a closer attention when characterizing residual stress. [8]

Contour Method

The contour method involves in cutting specimen into two pieces and measuring the structural deformation on the cut planes after residual stress has been relieved. The measured deformation data is being input to a finite element model to calculate residual stress at the surface of the specimen before cut. In the finite element model, the deformation data is imposed as a set of displacement boundary conditions on the model. The model accounts for material properties and geometry of the specimen as well as thermo data during the measurement to produce a comprehensive calculation of the residual stress. Specimens used for contour method are typically metals and they are being cut by electric discharge machining (EDM) method which induces minimum cutting stress. [9]

The contour method follows a superposition principle as shown in Figure 2. The step A shows the original one quarter of uncut specimen with residual stress in the structure. In step B, the specimen is cut in half at x=0 and the residual stress is being released. In step C, stress is being applied on cut surface and forces it back to its original shape like in step A. The amount of such applied stress is the amount of the residual stress that exists in the original specimen. This step is typically done by using the finite element model. [9]Steps mentioned above can be also described by Equation 2 in the following:

$$\sigma_A(x,y,z) = \sigma_B(x,y,z) + \sigma_C(x,y,z) \quad (1)$$

Where:

σ= entire stress tensor

A, B, C= different steps

Since there is not surface and shear stress at surface in step B, such superposition principle can be perfectly used for determining the original residual stress.

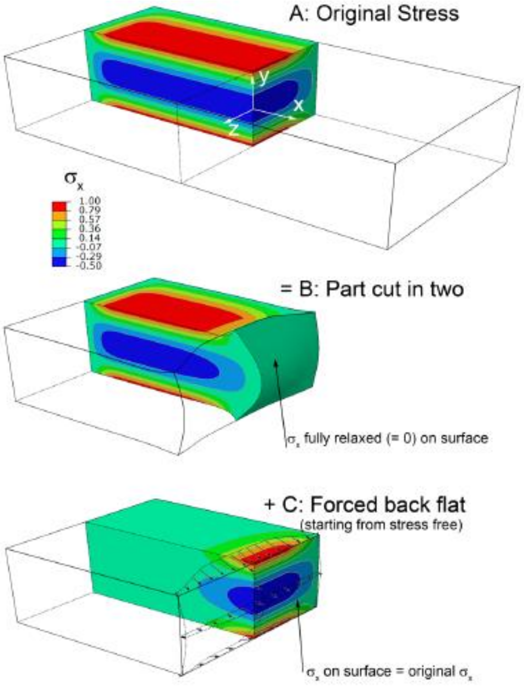

Figure 2. Superposition Principle for Contour Method; Stresses are Plotted on One Quarter of the Original Body [9]

Experimentally, after the specimen is cut like step B, the cut plane will be measured and the displacement data will be obtained in x direction only. This leads to the conclusion that stress being applied in step C will only be normal (in x direction) stress to the cut plane. Thus, the transversal displacements are not constrained. In the finite element model, the shear stress in xy and xz direction will be assumed zero when transversal displacements are not constrained. If there is any shear stress or transversal displacement appears, averaging two cut contours can cancel them out which results in only normal displacement exists at the cut plane. [9]

Cutting errors are main concerns of contour method since they can lead to wrong stress calculation. Anti-symmetric cutting effects may appear on the specimen that is cut in half. For example, one half may have more materials at one side while the other half has less. However, this type of error can be eliminated by averaging two contours as shown in Figure. 3. Such averaging step can be done in the software as MATLAB once two sets of displacement data are gathered. Another remarkable cutting error to be aware of is bulge error illustrated in Figure. 4. This error is a symmetric error that happens during cutting process. The cut is being made at a constant width w and as the cut proceeds, the stress relives and the materials at the tip of cut deform. The actual physical cut still has the width w which the width of materials being removed become reduced compared to the original state of body. When the plane is being forced back, the calculated stress is inaccurate since the material will not be return to its original location. However, such error can be minimized by clamping the specimen securely during cutting process. [9]

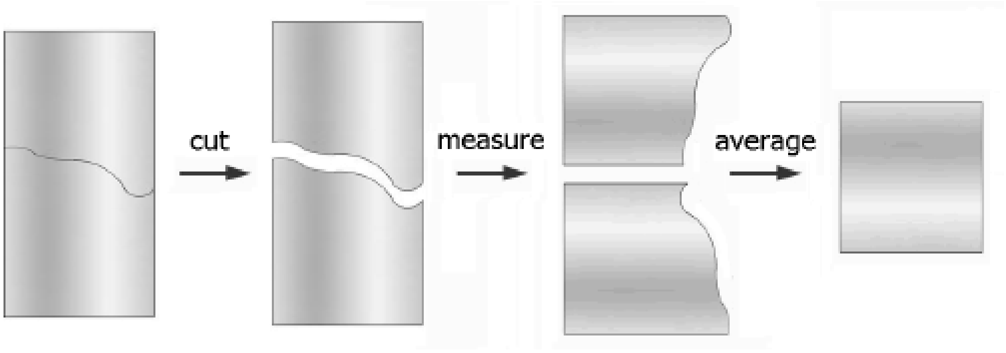

Figure 3. Averaging Two Contours to Eliminate Anti-symmetric Errors [9]

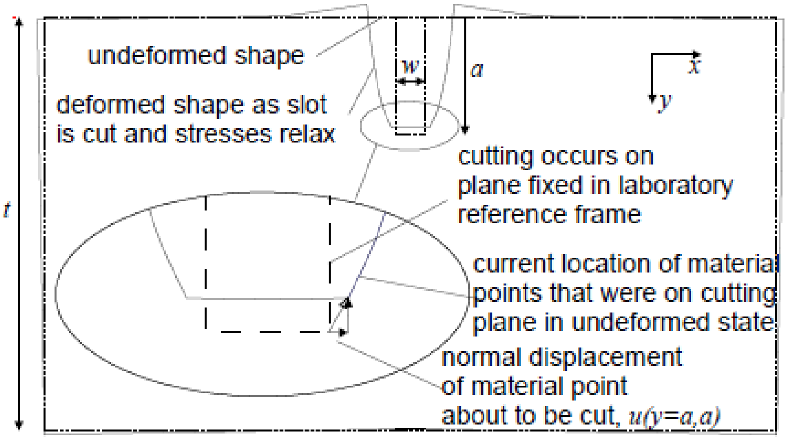

Figure 4. Bulge Error Effect [9]

X-ray Diffraction

The diffraction of X-ray occurs when the incident ray hits the atoms within the crystalline structure of the sample. The atoms then absorb such radiation and reradiate back with the same frequency at certain orientations. [10] The angle at which the strongest intensity of the radiation occurs can be desicbed by Bragg's Law shown below:

$$n\lambda = 2d \sin \Theta \qquad (2)$$

Where:

n=integer

d= inter-atomic spacing

λ=wavelength of radiation

Θ= Bragg angle

Figure 5 shown below illustrates the diffraction within a crystal structure. For X-ray diffraction, a range of angles are scanned and the angle where the highest intensity of the radiation occurs is selected to be the Bragg angle. As shown in Figure 6, either applied stress or residual stress can cause a shift in Bragg angle. Such shift causes small changes in the inter-atomic spacing which can then reflect the strain in irradiated area. The difference between such strain and the unstressed strain is used to calculate the residual stress.

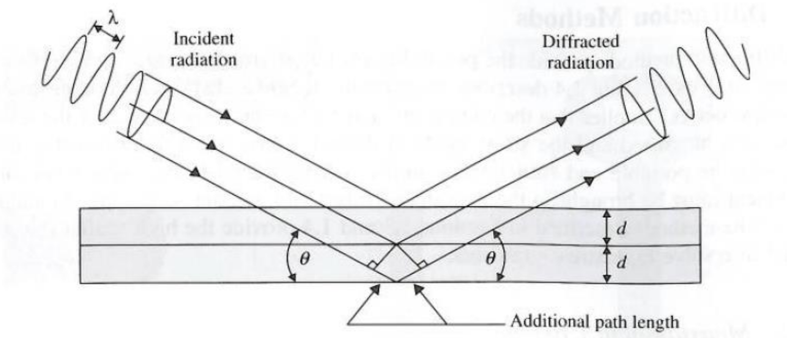

Figure 5. Diffraction within a crystal structure, d denotes for inter lattice spacing, Ө denotes for Bragg angle, λ denotes for wavelength. [10]

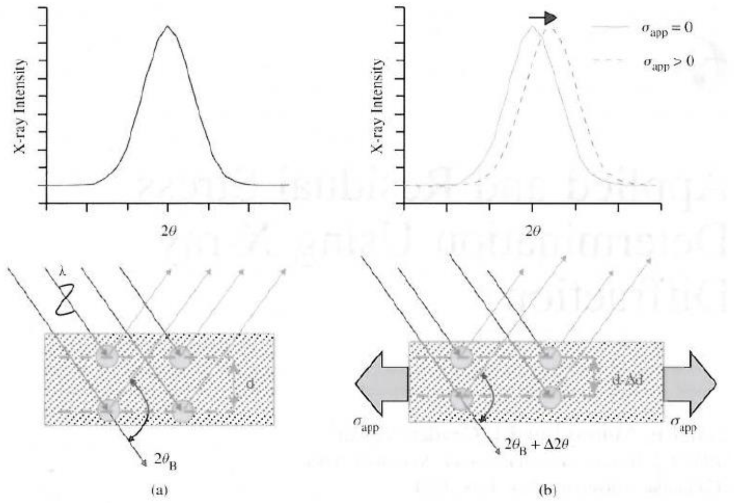

Figure 6.Schematic of X-ray diffraction on (a) unstressed state and (b) stressed state under applied load. [10]

X-ray diffraction method is commonly used to examine surface stress since it can only penetrate about a few microns deep inside of the specimen. The radiation is typically coming from an anode source or target of X-ray tube, for example, copper, chromium, and iron with wavelength of 0.7-2 angstroms can be used. Since the penetration is really shallow, the normal stress to the plane is considered to be zero. This simplifies the stress strain-strain equations which the unstressed lattice spacing does not need to be precisely known. The difference between specific lattice planes at several angles to the surface plane can be used to extrapolate the strain condition to a vector in the plane of the surface. [10]

Two techniques can be used to measure strain and stress through X-ray diffraction [10]:

1. Determining the elastic strain by measuring the atomic lattice spacing along different orientations using a diffractometer. These strains then undergo the transformation law for second rank tensors to compute strain tensors in the specimen coordinate. The stresses can then be calculated through Hooke's Law. This technique can be used in either single crystal structures or polycrystalline structures.
2. Determining the local and global curvatures of single-crystal sample through tracking the orientation of a crystal direction as a function of position within the sample using a goniometer equipped with a translation gage. If these curvatures are caused by the elastic constraints within the sample, the stresses can be calculated by using various formulas such as the Stoney Formula.

Neutron Diffraction Method

Neutron diffraction method also uses radiation penetrating technique to measure deformed strains caused by residual stress. Unlike in X-ray diffraction which the radiation interacts with the atoms in the crystal structure, in neutron diffraction, the neutrons are emitted to interact directly with the nucleus of the atoms. The diffracted intensity interacts with the electrons. Neutron diffraction also allows the radiation to penetrate in cm range deep inside the material which bulk stress can be measured. Neutrons are generally produced from fission or spallation and neutron energy usually provides 0.3 to 7 Angstroms for wavelength. Neutron diffraction allows the measurement of residual stress of samples that can have 0.1-1.5m thickness with a spatial resolution less than 1 mm which it does not require materials removal from the samples. Compare to X-ray diffraction method, neutron diffraction method also uses Bragg angle to calculate lattice spacing. The difference in lattice spacing indicates the change in strain which the residual stress can be calculated. However, neutron diffraction provides measurement of 3-dimensional stress which the unstressed lattice spacing must be precisely known. [11]

In neutron diffraction, the Bragg law can be written as Eq.3 where hkl denotes the Miller indices that indicate the planes of atomic lattice. Such equation requires the normal of <hkl> to diffracting planes lies on the angle bisector of the angle between the incident beam and the diffracted beam as shown in Figure 7. Grains whose planes normal <hkl> do not lie on the bisector are not being diffracted. [11]

$$\lambda=2d_{hkl}\sin \Theta_{hkl} \quad (3)$$

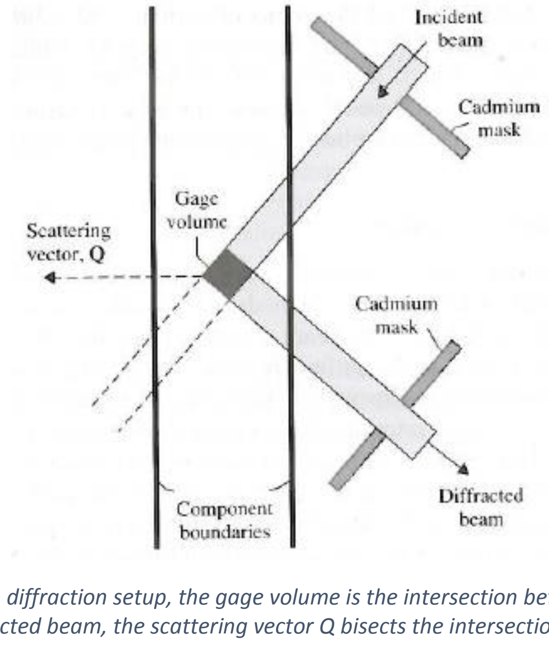

Figure 7. . Schematic of neutron diffraction setup, the gage volume is the intersection between the incident beam and the diffracted beam, the scattering vector Q bisects the intersection. [11]

Hole Drilling Method

Hole drilling method is a semi-destructive method which requires the material removal from the sample. Once the hole is been drilled on the sample, the material removal in such hole causes the redistribution of local residual stress. Figure 8 illustrates the schematic of hole drilling method. The relieved stress, either tensile or compressive, causes deformation to the strains and the deformed strains are measured by the strain gage that is being attached on the sample surface. Different designs of strain gage rosettes shown in Figure. 9, are developed to accommodate measuring of diffident types of residual stress. Optical measurement techniques such as Digital Image Correlation can also be used to calculate residual stress. Compare to strain gage measurement techniques, optical measurement techniques provide more accurate stress data and large stress calculation but they also relatively cost more. [12]

Before the specimen is being drilled, it undergoes multiple steps. Depending on the specimen size and hole dimension, the strain gage used can be varied. The specimen's surface then needs to be processed since the surface with high smoothness can form a good bonding with strain gage. After the surface preparation, the strain gage is then being wired on the surface and calibration of the gage is required. Lastly, the specimen is being put on the drilling machine and the different sized cutters can be chose for desired outcome. Two types of hole drilling machines are illustrated in Figure 10. [12]

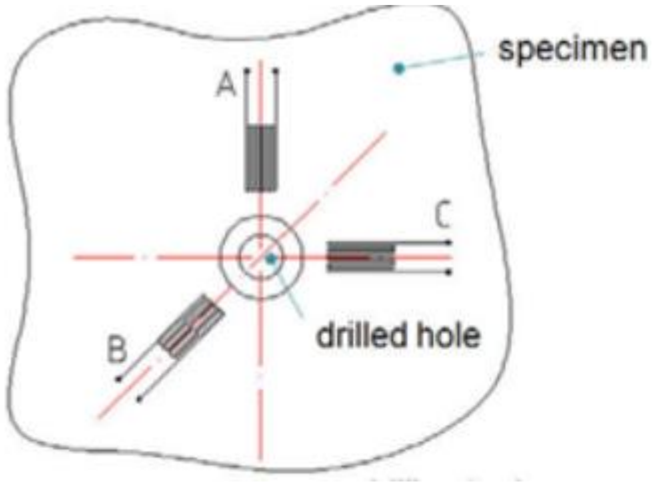

Figure 8. Schematic of Hole Drilling Method, A, B, C Denote the Strain Gage.

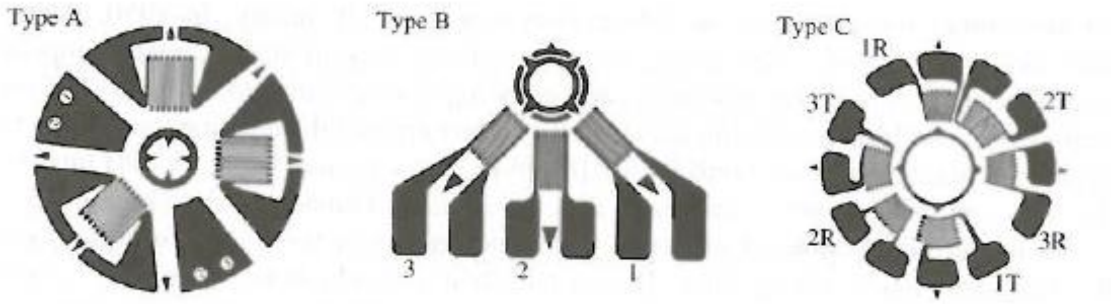

Figure 9. Standardized Hole Drilling Strain Gage Rosettes [12]

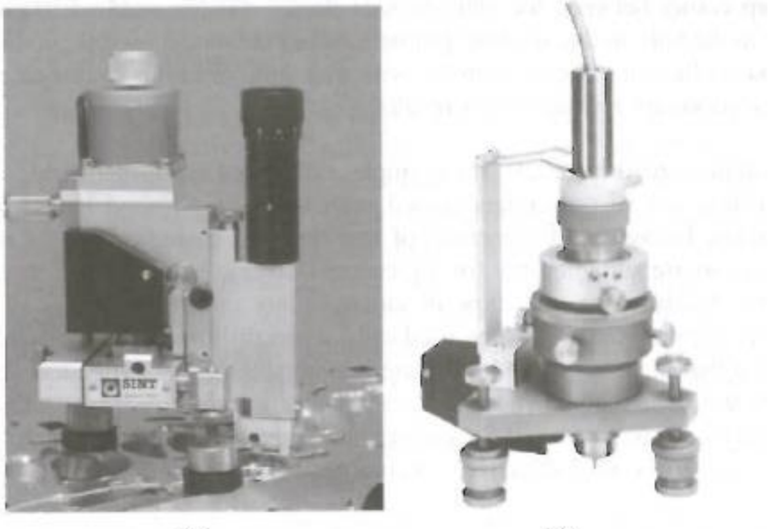

(a) (b)

Figure 10. Hole drilling machines (a) SINT MTS 3000 and (b) Micro-Measurement RS-200 [12]

Methodology

Various material properties were characterized for the stainless steel samples for better understanding of the materials and accurate stress calculation.

Young’s Modulus

In order to compare and confirm results with parallel tensile testing, we wanted to measure the Young’s Modulus of the stainless steel sample by another method. The acoustic method where the Young’s Modulus of the material is calculated from density, poisson ratio and the velocity of sound in the material was selected. The velocity of sound in a material is influenced by many factors including the Young’s modulus of the material, which means that the Young’s modulus of a material can be calculated if given the velocity of sound in that material. The Young’s modulus is given by

$$\mathrm{E} = \frac{V^2\rho(1+v)(1-2v)}{1-v} \tag{4}$$

Where V is the velocity of sound, ρ is the density of material and v is the Poisson ratio of the material. For this measurement, both ρ and v are taken from literature that ρ=7778kgm^{-3} and v=0.27.

The velocity of sound in the material is measured by GE USN 60 Ultrasonic Portable Flaw Detector, Krautkramer. A single element probe N5198 of frequency 10MHz was used in couple. The auto calibration feature of USN 60 was used to calculate velocity of sound and the values obtained are readings displayed on USN 60. Two pieces of sample of same stainless steel but with different thickness were required for such calibration. Their thicknesses were measured with a Vernier Caliper (0.001 inch). Calibration was performed five times and the average of the velocity of sound was 5740±4ms^{-1}.

Macro and Micro Hardness

Both macro and micro hardness tests were done on 304 stainless steel samples with different sizes. A sample with large size (18 cm*15cm*2cm) which is shown in Figure 11, was used for Rockwell hardness test at C scale with a load of 150 kgf. Eight samples with smaller size (2cm*2cm*2cm) in Figure 12 were used for Vickers hardness test. On each sample, the hardness measurements were taken at four points and the average hardness at these four points was used as the final hardness value for that sample. By using multiple small samples, the micro hardness could be measured at different spots which the unity of the hardness was determined.

Figure 11. AISI 304 Stainless Steel Sample with Large Size

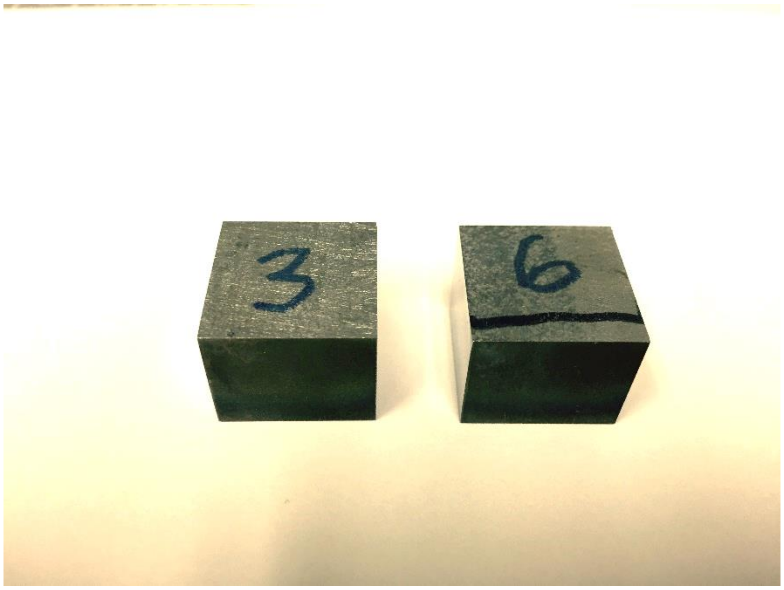

Figure 12. AISI 304 Stainless Steel Sample with Small Size

Microstructure

Microstructure characterization was done on mounted samples. The samples were polished by using multiple grits (240, 300,300, 600, and 1200) to obtain a mirror finish and then etched electrochemically in oxalic acid. The etched samples were being characterized under optical microscopy. Figure 13 shows the sample being etched in electro etching machine.

Figure 13. Electrochemical Etching

Phase Identification by Using X-ray Diffraction

A medium-size sample, shown in Figure 14, was used for phase identification by using X-ray diffraction. Table 2 below lists some of the parameters being used during the measurement. The phases in the samples were determined as well as the peak location at the highest 2θ value. Such 2θ value will be used for stress measurements later. The phase diagram obtained then being loaded into a software named HighScorePlus by PANalytical. This software was able to identify the phases within the sample as well as calculate their weight percentage content.

X-ray Instrument Type	PANalytical Empyrean Multipurpose X-ray Diffraction Instrument
X-ray Tube	Chromium
Tube Wavelength	2.29171 angstroms
Focus Type	Line
Mask Height	10 mm
Anti-scatter Slit	1 degree
Angle Range	60-135 degree
Total Time Duration	21 minutes

Table2. Parameters Used for Phase Identification in X-ray Diffraction

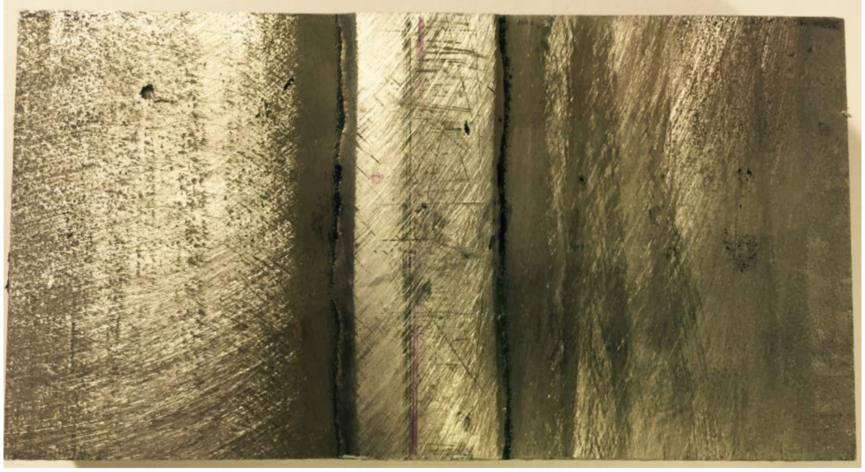

*Figure 14. AISI 304 Medium-size Sample with a Dimension of 10cm*5cm*2cm*

Sample Annealing & Strain-free Lattice Parameter Determination

Three small samples were annealed for one hour in the furnace at two different temperatures: 870 degree Celsius and 1100 degree Celsius. The samples were immediately cold water quenched after annealing. The purpose of such experiment was to determine the lattice parameter, a, in a stress free state. For AISI 304 stainless steel, a stress relieving annealing temperature is around 875 degree Celsius. [13] The normalizing temperature is in the range of 1038 to 1121 degree Celsius. It is expected that the residual stress remained in the sample would be fully relieved at a temperature above 600 degree Celsius. [7] After quenching, an X-ray diffraction analysis was done on all samples with the same parameters listed in Table 2 above. Once the highest peak location was determined for all samples, the Bragg Law which was shown in Eq. 2, was used to calculate d-spacing. Once the d-spacing values were obtained, the strain-free lattice parameter could be obtained from Eq.5.

$$\frac{1}{d^2} := \frac{h^2 + k^2 + l^2}{a^2} \tag{5}$$

Where:

d= d-spacing

a= lattice parameter

h,k,l= Miller Indices

Stress Measurement by X-ray Diffraction

The stress measurements done by using X-ray diffraction used parameters in Table 3.

X-ray Instrument Type	PANalytical Empyrean Multipurpose X-ray Diffraction Instrument
X-ray Tube	Chromium
Tube Wavelength	2.29171
Focus Type	Point
Mask & Slit Dimension	10mm * 3mm
Number of ϕ	3 (0, 45, 90 degree)
Number of ψ	11 (0, ±18.43, ±26.57, ±33.21, ±39.23, ±45 degree)
Scan Mode	2θ+Ω
Measured Angle Range	1.96

Table 3. Parameters for XRD Stress Measurements

Such measurement plan would yield a total of 33 results for one measurement point due to different combinations of angle ϕ and φ. Two data sets were obtained under such measurement plan. As shown in Figure 15 below, the first set of data was obtained at 0.5 cm below the centerline of the sample. The second set of data was acquired at 1 cm above the centerline. Each data set contained 17 points whereas each black point was 1 cm apart with a purple point in between that was 0.5cm apart from black point on each side. Figure 16 provides a schematic of stress measurement by using 2θ-Ω mode. In the real experiment, the source would come from left direction rather than right direction shown in Figure 17. The source and the receiver would rotate along both 2θ and Ω axis. In Figure 16, the σ_{11} direction represented transverse direction on the sample; the σ_{22} direction represented longitudinal direction; the σ_{33} direction represented normal direction. Figure 18 provides the clearer stress directions on the real sample. Strain data from all three directions were desired to use to calculate three principal stresses. A measurement angle range has been chosen to be very small because we were only interested in the region where the highest intensity occurred. The location with the highest intensity would help us to locate the peak accurately. The inclusion of other regions with lower intensity may cause peak diagram shift when calculating in software especially when there was a second phase or background noise present at the peak, thus resulting in wrong peak location. Our stress measurement process carefully followed the ASTM standards. [14]

Figure 15. Medium-size Sample with Measurement Points

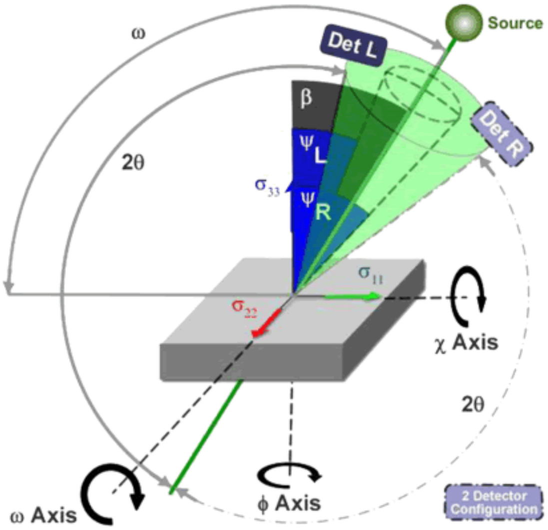

Figure 16. Schematic of Stress Measurement in XRD [14]

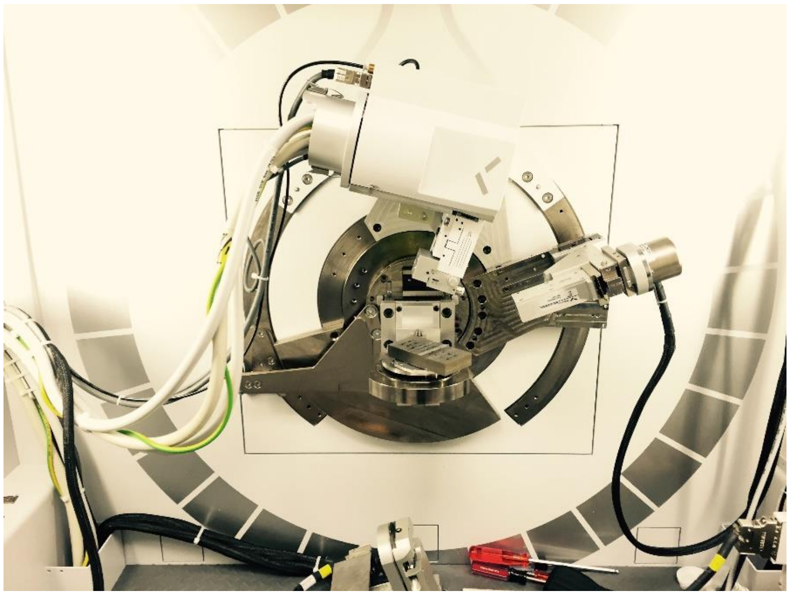

Figure 17. Actual Experimental Setup

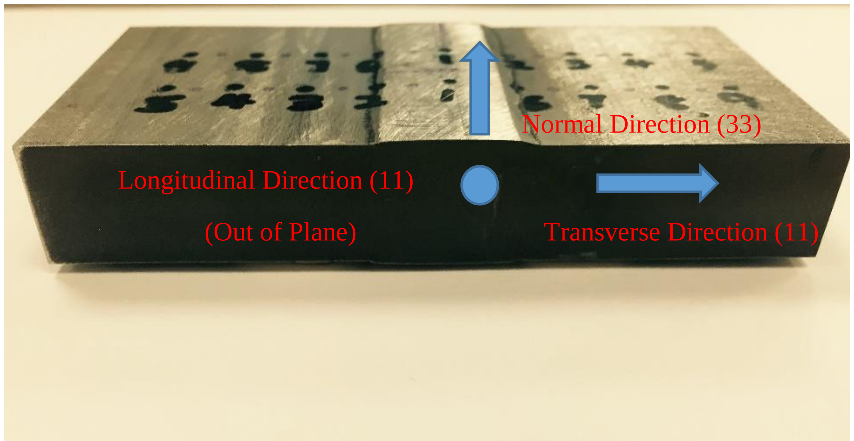

Figure 18.Strain Directions on Actual Sample

The measured strain data sets were then being loaded into the software called StressPlus by PANalytical. Such software was able to locate the accurate peak location for each measurement point as well as generate d_ψ vs. $\sin^2 \psi$ diagrams for stress calculation later. The background was subtracted and the Lorentz-Polarization-Absorption factor was applied to each measurement to enhance the accuracy of the peak location. [14]

The Eq.6 and Eq.7 are the fundamental equations of the stress calculation for X-ray Diffraction. [10]

$$\varepsilon_{\phi\varphi} := \frac{\left(d_{hkl}\right) - d_0}{d_0} \tag{6}$$

$$\varepsilon_{\phi\varphi} := \varepsilon_{11}\cdot\cos^2(\phi)\cdot\sin^2(\varphi) + \varepsilon_{12}\cdot\sin(2\cdot\phi)\cdot\sin^2(\varphi) + \varepsilon_{22}\cdot\sin^2(\phi)\cdot\sin^2(\varphi) + \varepsilon_{33}\cdot\cos^2(\varphi) + \varepsilon_{13}\cdot\cos(\phi)\cdot\sin(2\cdot\varphi) + \varepsilon_{23}\cdot\sin(\phi)\cdot\sin(2\cdot\varphi) \tag{7}$$

Where:

ϕ and ψ = rotational angles
hkl = Miller indices
$(d_{hkl})_{\phi\psi}$ = deformed d-spacing at peak interested
d_0 = unreformed d-spacing
ε_{ij} = strain in six different directions

There are two different stress states. One is biaxial stress state which there only exists σ_{11} (transverse) and σ_{22} (longitudinal) stress. On the other hand, the triaxial stress state has a normal stress in σ_{33} direction as well as shear stress in σ_{12} and σ_{13} direction. To differentiate the two stress states, a closer look is needed to the d_ψ vs. $\sin^2 \psi$ diagram. If the diagram looks like Figure 19, where the linear relationship exists at both positive and negative ψ, it indicates a biaxial stress. If the diagram is similar to Figure 20, then it suggests a triaxial stress state. The formulas for stress calculation are different for two stress states. [15]

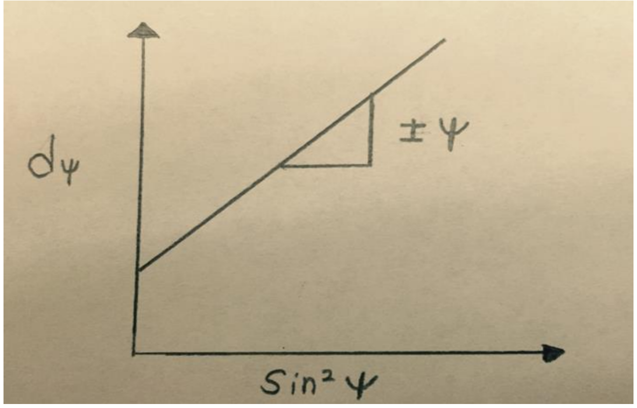

Figure 19. Biaxial Stress State with Linear Behavior

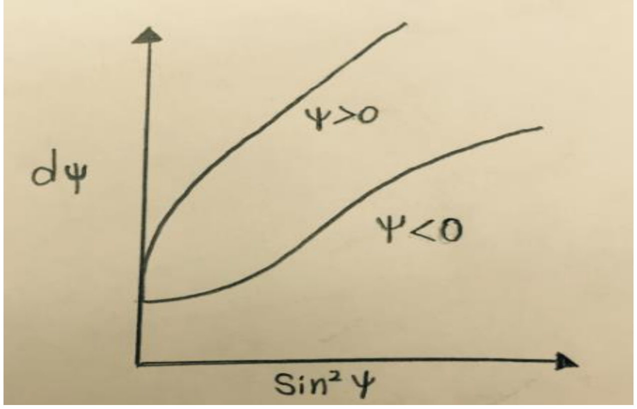

Figure 20. Triaxial Stress State- ψ Splitting Behavior

For a biaxial stress state, Eq.8 should be used along with the d_ψ vs. $\sin^2 \psi$ diagram. [15]

$$d_{\varphi} := \frac{1+v}{E}\cdot d_0\cdot\sigma_{\phi}\cdot\sin^2\varphi - \frac{v}{E}\cdot\left(\sigma_{11}+\sigma_{22}\right)\cdot d_0 + d_0 \tag{8}$$

Where:

d_0 = strain-free d-spacing

σ_ϕ= stress in ϕ direction

v= Poisson's ratio

E= elastic modulus

The slope of d_ψ vs. $\sin^2\psi$ diagram could be obtain through a linear regression fit in Excel or MATLAB. Such slope could be applied to Eq.9 below to obtain $\sigma_{\phi.}$ [15]

$$m := \frac{1+v}{E}\cdot d_0\cdot\sigma_{\phi} \tag{9}$$

Once the stress along ϕ was obtained, σ_{11}, σ_{22}, and σ_{12} were calculated through Eq.10 by applying different ϕ values (In our case, ϕ= 0, 45, 90 degree). [15]

$$\sigma_{\phi} := \sigma_{11}\cdot\cos^2\phi + \sigma_{12}\cdot\sin 2\cdot\phi + \sigma_{22}\cdot\sin^2\phi \tag{10}$$

For the triaxial stress state, parameters a_1 and a_2 needed to be calculated to obtain stress. [15]

$$a_1 := \frac{d_1+d_2}{2\cdot d_0} - 1 = \left(\varepsilon_{11}\cdot\cos^2\phi + \varepsilon_{12}\cdot\sin 2\cdot\phi + \varepsilon_{22}\cdot\sin^2\phi - \varepsilon_{33}\right)\cdot\sin^2\varphi + \varepsilon_{33} \tag{11}$$

Where:

d1= d-spacing at $\varphi>0$ at each $\phi\psi$ combination

d2= d-spacing at $\varphi<0$ at each $\phi\psi$ combination

Once parameter a_1 was obtained through various d-spacing values, a plot was created for a_1 vs. $\sin^2\psi$. The slope of such diagram could be used to obtain strain in 11, 22, and 12 direction (at ϕ= 0, 45, 90 degree) by using Eq.12 Strain in 33 direction was obtained by using d-spacing at φ=0 and ϕ= 0, 45, 90. Note that all three d-spacing values at φ=0 should be the same and such phenomenon would indicate if any misalignments of the instrument exist in the system. [15]

$$m_{a1} := \varepsilon_{11}\cdot\cos^2\phi + \varepsilon_{12}\cdot\sin 2\phi + \varepsilon_{22}\cdot\sin^2\phi - \varepsilon_{33} \tag{12}$$

Parameter a_2 could be generated by using Eq. 13. [15]

$$a_2 := \frac{d_1 - d_2}{d_0} = \left(\varepsilon_{13}\cdot\cos\phi + \varepsilon_{23}\cdot\sin\phi\right)\cdot\left|\sin 2\varphi\right| \tag{13}$$

Once a_2 was obtained from Eq.13, a plot was created for a_2 vs. sin $|2\varphi|$. The sloped was extracted from the linear fitted line and it could be applied to Eq.14 to obtain shear strains in 12 direction (ϕ=0) and 23 direction (ϕ=90). [15]

$$m_{a2} := \varepsilon_{12}\cdot\cos\phi + \varepsilon_{23}\cdot\sin\phi \tag{14}$$

All strains acquired were used to calculate stress in different directions by multiplying them with elastic modulus and one plus Poisson ratio.

Results and Discussion

Elastic Modulus

According to Eq.1 the E was calculated to be 205GPa. Assuming ρ and v were exact values, the error involved in measurement is about 0.1%.

Macro and Micro Hardness

The macro harness of the sample was obtained at the value of 9 at C scale. The micro hardness data was acquired from eight small samples which were EDM cut from the big one and the result is shown in Figure 21.

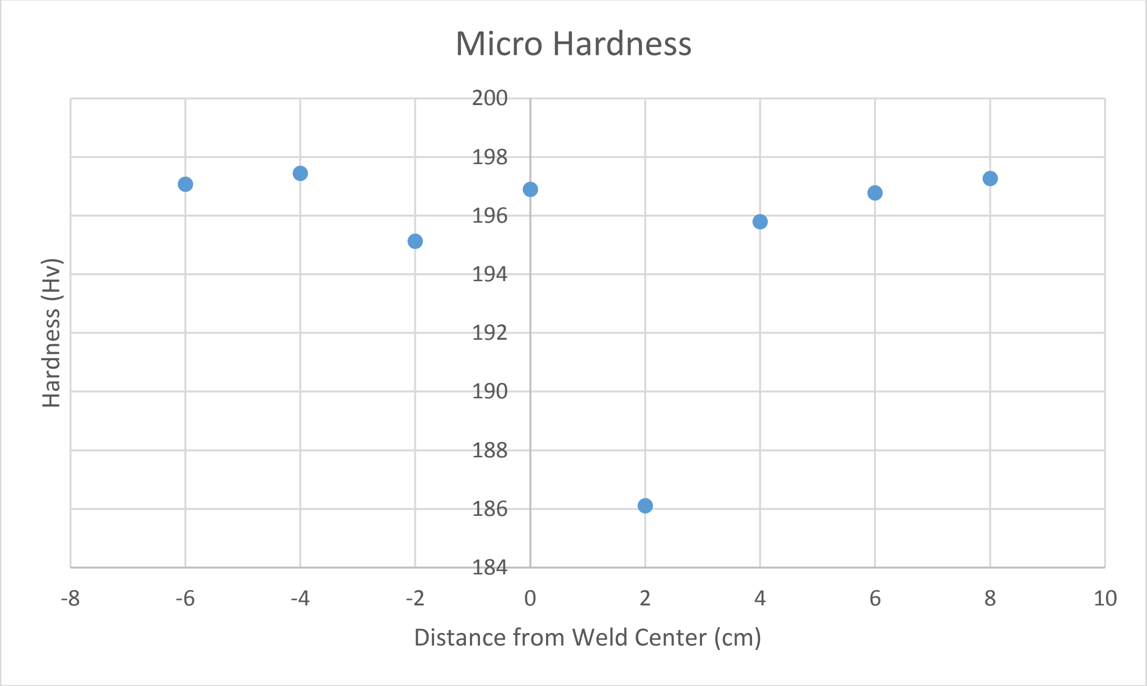

Figure 21. Micro Hardness on Eight Small Samples

According to both hardness results, it has been confirmed that the stainless steel samples have been annealed which the materials were really soft.

Microstructure

The mounted sample was being etched electrochemically in oxalic acid for 13 minutes. The microstructure of the sample presented clearly after etching as shown in Figure 22. The annealing twins were apparent and the majority of the region appeared to be austenite. Such microstructure diagram shared the same characteristics with other diagrams in different literatures. [16] The black dots existed in the figure were caused by over polishing since they did not exist after the first few rounds of polishing.

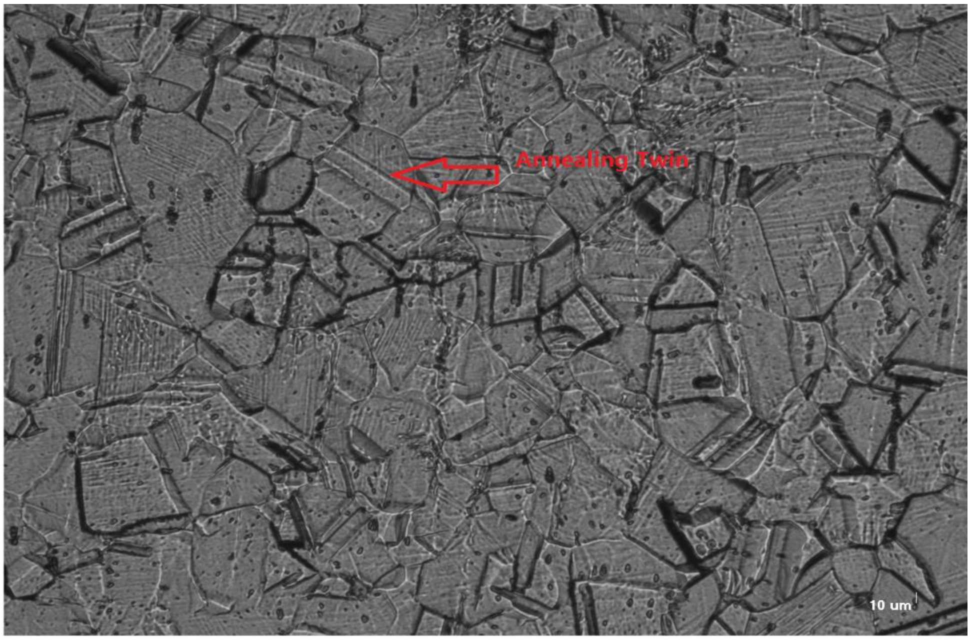

Figure 22. Microstructure of AISI 304 Stainless Steel Sample

Phase Identification

Figure 23 below shows the phase identification diagram of the stainless steel sample. The red dots represents the actual measurement while the blue continuous line was fitted by using Rietveld refinement in HighScorePlus software. [17] As shown in the diagram, most of the peaks are overlapping between measured and experimentally fitted data. However, at a higher 2θ degree, the shift between the peaks becomes obvious. This is due to the distorted strain caused by residual stress in the real sample which it shifts the peaks at higher 2θ values. The graph below the phase identification diagram shows the deviation of the intensity between measured and experimentally calculated data.

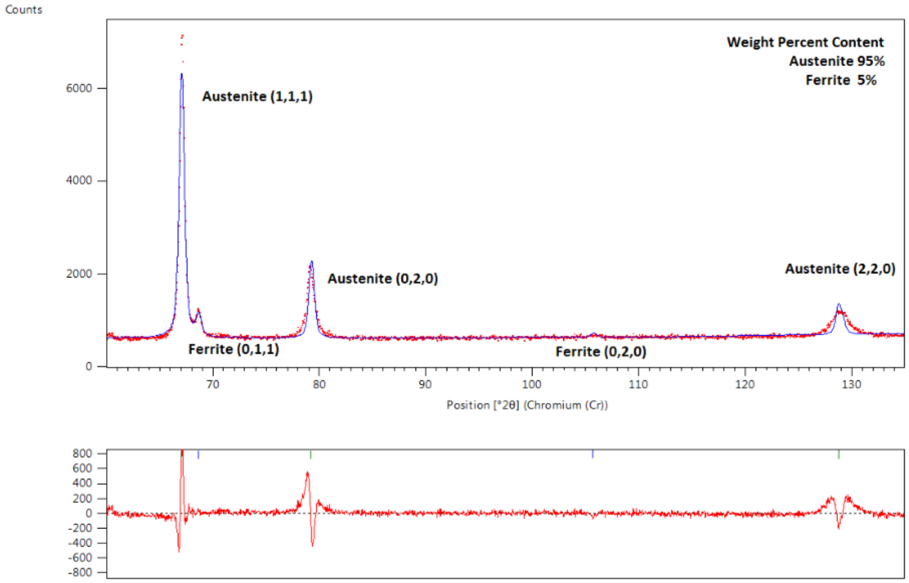

Figure 23. Phase Identification Diagram of AISI 304 Sample

From the phase identification diagram, we identified the highest 2θ value where the peak presented. Such values was approximated to be 128.7 degree and was used it as 2θ parameter for stress measurement.

Strain Free Lattice Parameter

Three samples were annealed at different temperatures. The first sample was annealed at 870 degree Celsius for an hour and water quenched immediately after annealing. The sample was then being cut to expose the surface without oxidation. To obtain a better surface finish, the sample was then being polished. The strain-free lattice parameter was determined by X-ray diffraction and calculated as 3.59617 angstroms. The second sample was annealed at 870 degree Celsius for an hour and followed the same procedure as the first one without the polishing step. The strain-free lattice parameter obtained as 3.59361 angstroms. The third sample was annealed at 1100 degree Celsius for an hour and followed the same procedure as the second one. The strain-free lattice parameter obtained as 3.59253 angstroms. In the other two literature references, we found that strain-free lattice parameters of stainless steel were 3.5918 angstroms and 3.6114 angstroms. Due to slightly chemical component difference and various machining processes for different stainless steel samples, it was safe to assume that any strain-free parameters in the range of 3.5918 to 3.6114 were acceptable for AISI 304 stainless steel. All three measured values fell into this range but we preferred the second and third value since polishing may induce some stress to the sample. Table 4 lists the d-spacing values with their respective lattice parameters.

A(lattice parameter, angstroms)	D_0 (strain-free d-spacing, angstroms)
3.59617 (annealed @880 C, polished)	1.27189
3.59361(annealed @ 880C)	1.27053
3.59253 (annealed @ 1100C)	1.27015
3.5918	1.26989
3.6114	1.27682

Table 4. D-spacing Values with Their Respective Strain-free Lattice Parameters

For the stress calculation in this project, the values of d_0 were chose to be 1.27053 for data set one and 1.27015 for data set two.

Stress Calculation

Among the measured data, almost all the measured points possessed d_ψ vs. $\sin^2 \psi$ diagrams that were similar to either Figure 24 or Figure 25, which both of them indicates a triaxial stress state. In Figre 24, two sets of data are close to each other in the same trend which indicated that there is a small shear stress. On the other hand, Figure 25 shows that two sets of data are slightly further apart which suggested a bigger shear stress value. However, due to the insignificance of the shear stress to the problem we were interested in and small values of such stress, its results and calculations were not included in this report.

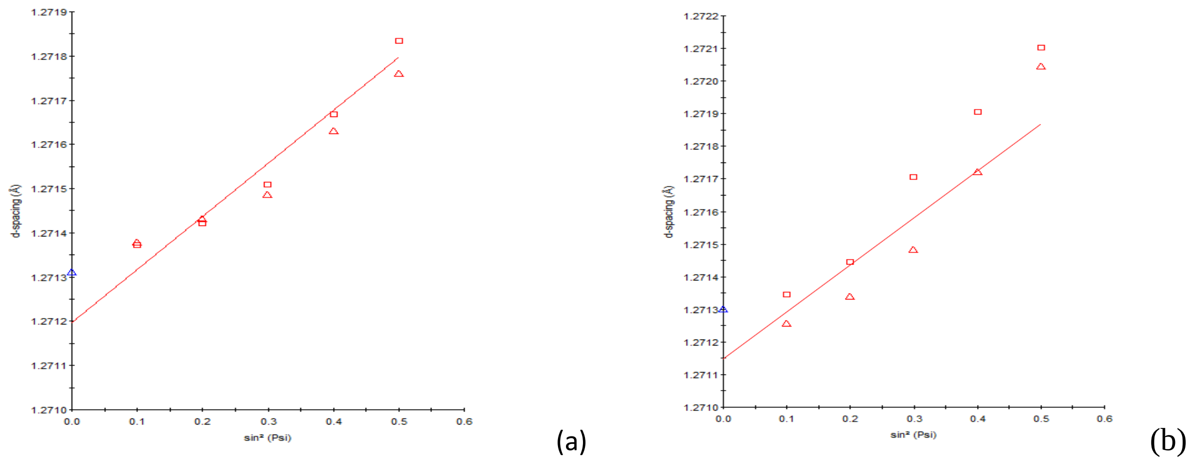

Figure 24. (a) Linear Behavior with Small Shear Stress; (b) ψ Splitting Behavior with Larger Shear Stress (triangle indicates data measured at positive ψ and square indicates data measured at negative ψ)

Normal Stress

Normal stress plays an important role in determining transverse stress and longitudinal stress according to Eq. 15. It is the formula for calculating normal strain.

$$\varepsilon_{33} := \frac{d_{\phi\varphi} - d_0}{d_0} \qquad (15)$$

In this formula, three $d_{\phi\varphi}$ were measured at φ=0 and ϕ=0, 45, 90. All three values should be the same or varied slightly to check if the instruments have any errors. [10]

Stress Measurements

Set One

Normal Stress

Table 5 includes the value of normal stress at each measured point. Figure 25 provides a clearer trend of normal stress across the sample. The strain free d-spacing value used was 1.270533 for stress calculations in all three directions. Table 6 includes d-spacing values measured at φ=0 for normal stress calculation.

Distance from Center of the Weld (mm)	Normal Residual Stress (MPa)
-40	303.30

-35	267.90
-30	249.99
-25	220.70
-20	233.61
-15	-55.32
-10	192.61
-5	106.56
0	310.86
5	144.26
10	226.22
15	138.16
20	130.54
25	154.52
30	168.03
35	155.17
40	162.69
Standard Deviation	± 26

Table 5. Normal Stress for Set One

Distance from Weld Centerline (mm)	Strained d-spacing(angstroms)	Strain-free d-spacing(angstroms)
40	1.271327	1.270533
35	1.27129	1.270533
30	1.271353	1.270533
25	1.271287	1.270533
20	1.27117	1.270533
15	1.271207	1.270533
10	1.271637	1.270533
5	1.271237	1.270533
0	1.27205	1.270533
-5	1.271053	1.270533
-10	1.271473	1.270533
-15	1.270263	1.270533
-20	1.271673	1.270533
-25	1.27161	1.270533
-30	1.271753	1.270533
-35	1.27184	1.270533
-40	1.272013	1.270533

Table 6. D-spacing Values at $\varphi=0$

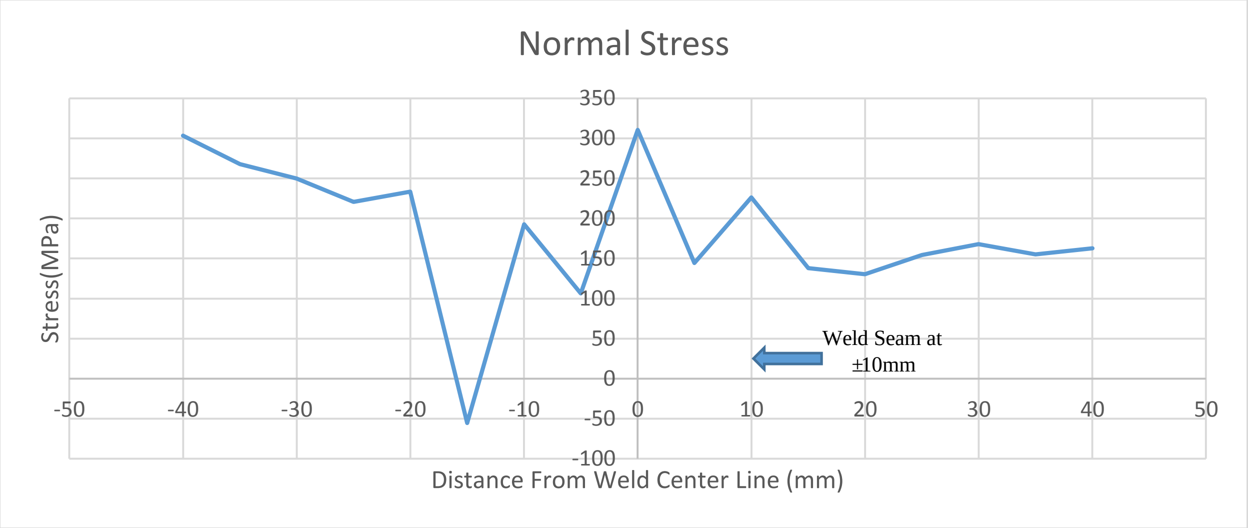

Figure 25. Normal Stress Distribution across the Sample

Transverse Stress

Table 7 and Table 8 provide the values of transverse stress with and without the presence of normal stress. The stress values were obtained by using StressPlus software when normal stress was missing. When taking normal stress into account, the stress values were acquired through calculations done by using Eq.11 to Eq.15 in Excel and MathCAD. Figure 26 provides a clearer trend of stress distribution.

Distance from Center of the Weld (mm)	Transverse Residual Stress (MPa)	Standard Deviation (MPa)
-40	142	16.46
-35	188.9	18.03
-30	188.7	21.27
-25	194.5	19.9
-20	141.9	15.92
-15	19.9	14.69
-10	18.1	18.34
-5	191.9	35.67
0	-115.9	23.87
5	92.7	28.58
10	5.1	24.57
15	90.5	14.17
20	99.2	19.3

25	96	20.11
30	95.9	19.56
35	162.9	17.81
40	149.1	13.68

Table7. Transverse Stress in Biaxial Stress State for Set One

Distance from Center of the Weld (mm)	Transverse Residual Stress (MPa)	Standard Deviation (MPa)
-40	641.76	26.34
-35	658.42	20.62
-30	640.46	24.97
-25	611.30	11.13
-20	514.71	33.45
-15	48.78	2.69
-10	114.50	2.37
-5	549.07	20.85
0	24.47	13.42
5	352.51	15.87
10	200.18	50.18
15	242.26	11.51
20	260.61	42.12
25	258.66	12.68
30	324.13	48.31
35	387.92	8.89
40	344.96	17.09

Table 8. Transverse Stress in Triaxial Stress State for Set One

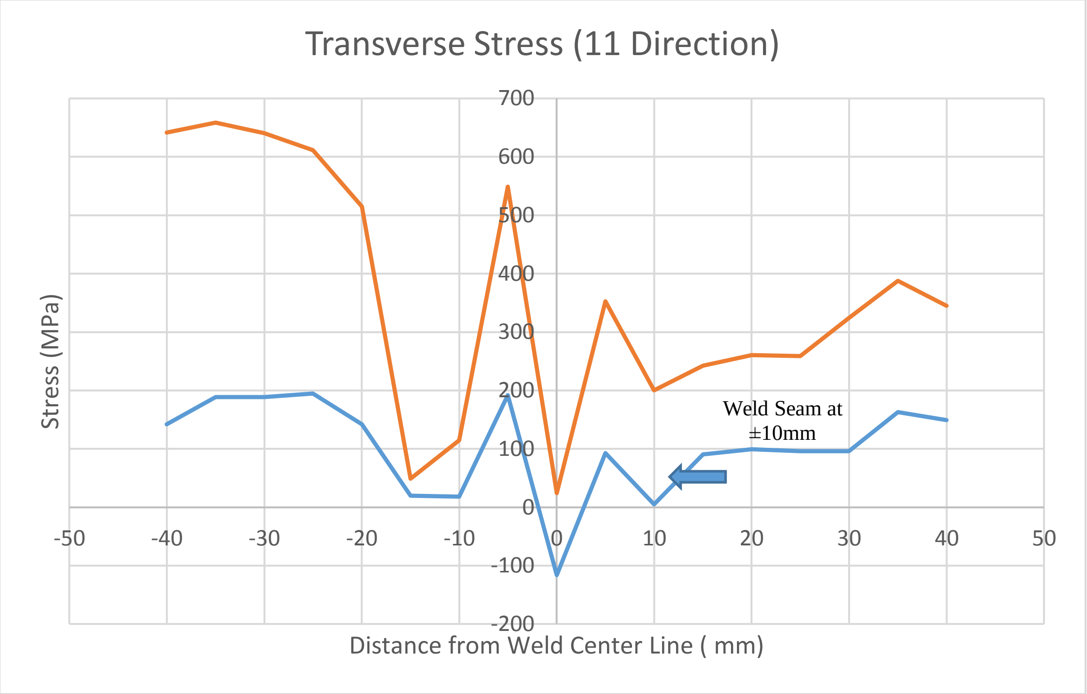

Figure 26. Transverse Stress Distribution across the Sample (orange line represents the triaxial state and blue line represents the biaxial state)

Longitudinal Stress

Table 9 and Table 10 provide the values of longitudinal stress with and without the presence of normal stress. The stress values were obtained by using StressPlus software when normal stress was missing. When taking normal stress into account, the stress values were acquired through calculations done by using Eq.11 to Eq.15 in Excel and MathCAD. Figure 27 provides a clearer trend of stress distribution.

Distance from Center of the Weld (mm)	Longitudinal Residual Stress (MPa)	Standard Deviation (MPa)
40	147.07	17.34
35	189.71	34.25
30	67.74	5.08
25	38.45	4.97
20	77.40	8.74
15	152.96	3.76
10	531.11	16.64
-5	366.83	17.02

0	50.50	3.96
5	222.36	12.98
10	486.59	30.43
15	580.58	44.45
20	520.96	84.20
25	544.91	38.50
30	584.49	13.28
35	545.69	11.62
40	553.24	13.59

Table 9. Longitudinal Stress in Triaxial Stress State for Set One

Distance from Center of the Weld (mm)	Longitudinal Residual Stress (MPa)	Standard Deviation (MPa)
40	-38.5	16.46
35	-11.5	18.03
30	7.5	21.27
25	30.3	19.9
20	13.4	15.92
15	48.7	14.69
10	106.8	18.34
-5	190.6	35.67
0	139.2	23.87
5	78.4	28.58
10	106.6	24.57
15	284.5	14.17
20	247	19.3
25	243.7	20.11
30	217.6	19.56
35	194.1	17.81
40	186.7	13.68

Table 10. Longitudinal Stress in Biaxial Stress State for Set One

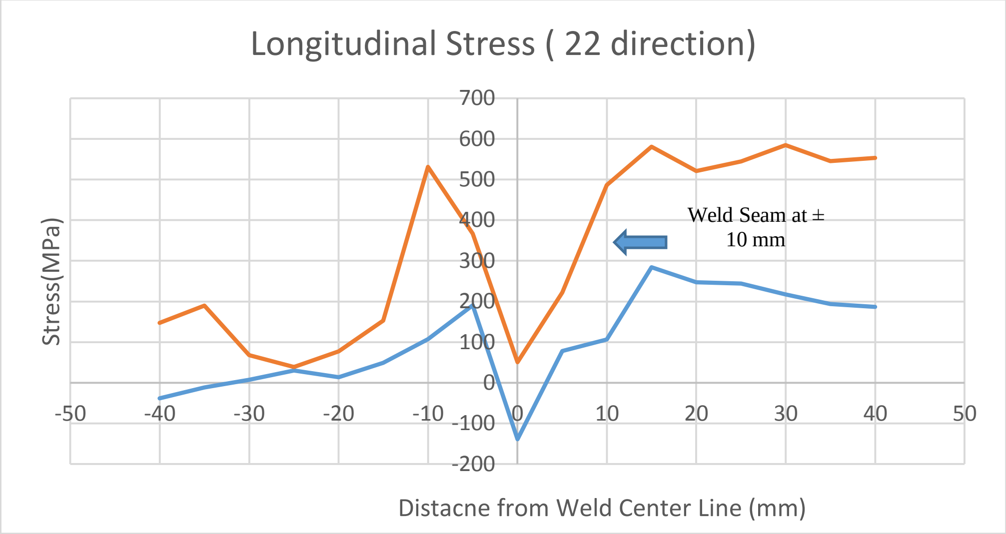

Figure 27. Longitudinal Stress Distribution across the Sample (orange line represents the triaxial state and blue line represents the biaxial state)

Set Two

Normal Stress

Table 11 includes the value of normal stress at each measured point. Figure 28 provides a clearer trend of normal stress across the sample. The strain free d-spacing value used was 1.27015 for stress calculations in all three directions. Table 12 includes d-spacing values measured at φ=0 for normal stress calculation.

Distance from Weld Centerline (mm)	Normal Stress (Mpa)
40	342.9
35	307.5
30	279.4
25	291.1
20	304.8
15	280.2
10	257.7
5	216.7
0	446.2
-5	234.3
-10	292.5
-15	211.1
-20	234.3
-25	219.3

-30	235.7
-35	252.1
-40	243.3
Standard Deviation (Mpa)	52

Table 11. Normal Stress Value for Data Set Two

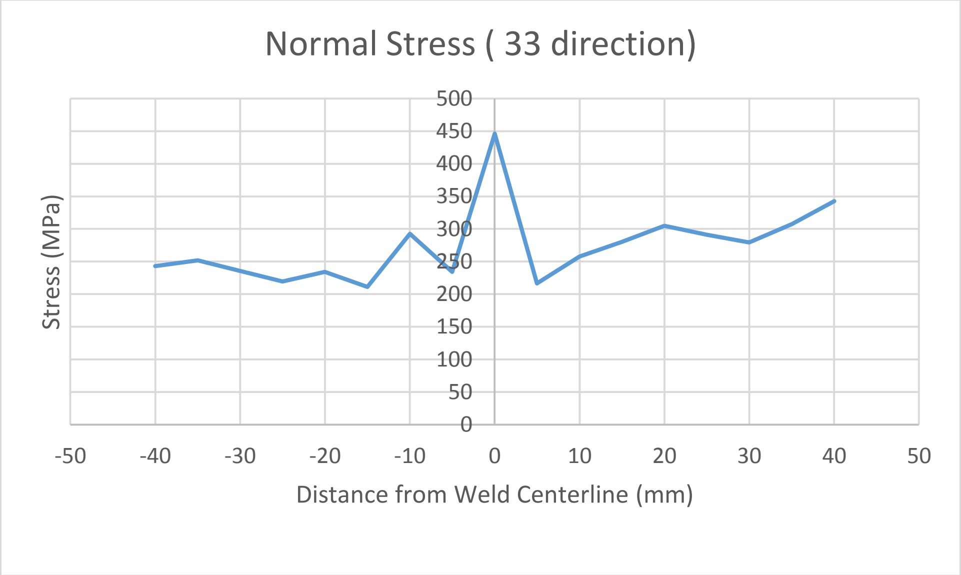

Figure 28.Normal Stress Distribution across the Sample

Distance from Weld Centerline (mm)	Strained d-spacing(angstroms)	Strain-free d-spacing(angstroms)
40	1.271823	1.27015
35	1.27165	1.27015
30	1.271513	1.27015
25	1.27157	1.27015
20	1.27637	1.27015
15	1.271517	1.27015
10	1.271407	1.27015
5	1.271293	1.27015
0	1.272327	1.27015
-5	1.271207	1.27015
-10	1.271577	1.27015
-15	1.27118	1.27015
-20	1.271293	1.27015
-25	1.27122	1.27015
-30	1.2713	1.27015
-35	1.27138	1.27015
-40	1.271337	1.27015

Table 12. D-spacing Values at φ=0

Transverse Stress

Table 13 and Table 14 provide the values of transverse stress with and without the presence of normal stress. The stress values were obtained by using StressPlus software when normal stress was missing. When taking normal stress into account, the stress values were acquired through calculations done by using Eq.11 to Eq.15 in Excel and MathCAD. Figure 29 provides a clearer trend of stress distribution.

Distance from Weld Centerline (mm)	Transverse Stress(MPa)	Standard Deviation (MPa)
40	131.1	14.11
35	213.3	18.01
30	236.4	24.32
25	219	20.14
20	148.3	16.68
15	51.9	12.84
10	45.9	23.57
5	143.6	49.09
0	-141.7	35.89
-5	24.1	29.86
-10	23.7	19.28
-15	72.6	13.13
-20	86.2	16.96
-25	104.9	19.42
-30	103.3	22.25
-35	148.4	17.76
-40	158.5	14.14

Table 13. Transverse Stress in Biaxial Stress State for Set Two

Distance from Weld Centerline (mm)	Transverse Stress(MPa)	Standard Deviation (MPa)
40	629.3	14.10
35	724	22.88
30	722	10.83
25	707.6	11.04
20	617.2	33.95
15	384.3	125.24
10	205.6	53.81
5	477	38.45
0	55.71	5.39
-5	130.1	3.63

-10	240.4	82.58
-15	367.3	0.26
-20	364.5	16.22
-25	349.5	45.75
-30	365.9	61.84
-35	434.4	22.68
-40	243.3	2.38

Table 14. Transverse Stress in Triaxial Stress State for Set Two

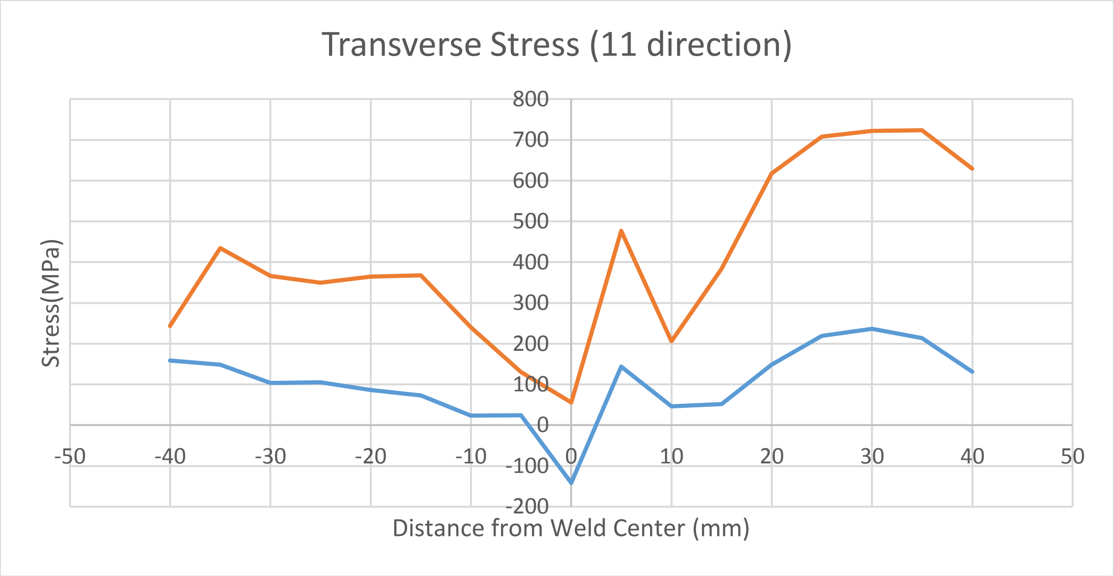

Figure 29.Transverse Stress Distribution across the Sample (orange line represents the triaxial state and blue line represents the biaxial state)

Longitudinal Stress

Table 15 and Table 16 provide the values of longitudinal stress with and without the presence of normal stress. The stress values were obtained by using StressPlus software when normal stress was missing. When taking normal stress into account, the stress values were acquired through calculations done by using Eq.11 to Eq.15 in Excel and MathCAD. Figure 30 provides a clearer trend of stress distribution.

Distance from Weld Centerline (mm)	Longitudinal Stress(MPa)	Standard Deviation (MPa)
40	-30.9	14.11
35	-9.2	18.01
30	16.3	24.32
25	16.6	20.14

20	15.3	16.68
15	78.6	12.84
10	139.7	23.57
5	120.6	50.27
0	-196.8	35.89
-5	24.9	29.86
-10	137.6	19.28
-15	298.3	13.13
-20	261.2	16.96
-25	287.7	19.42
-30	287.2	22.25
-35	214.6	17.76
-40	184.4	14.14

Table 15. Longitudinal Stress in Biaxial Stress State for Set Two

Distance from Weld Centerline (mm)	Longitudinal Stress(MPa)	Standard Deviation (MPa)
40	160.7	4.69
35	151.3	14.24
30	149.2	23.06
25	160.9	28.41
20	200.7	80.18
15	488.5	20.52
10	648.2	46.28
5	451	3.20
0	159.8	19.42
-5	390.5	139.96
-10	657	11.50
-15	679.8	38.14
-20	755	15.55
-25	688	46.16
-30	782.5	17.14
-35	590.6	54.22
-40	607.8	14.65

Table 6. Longitudinal Stress in Triaxial Stress State for Set Two

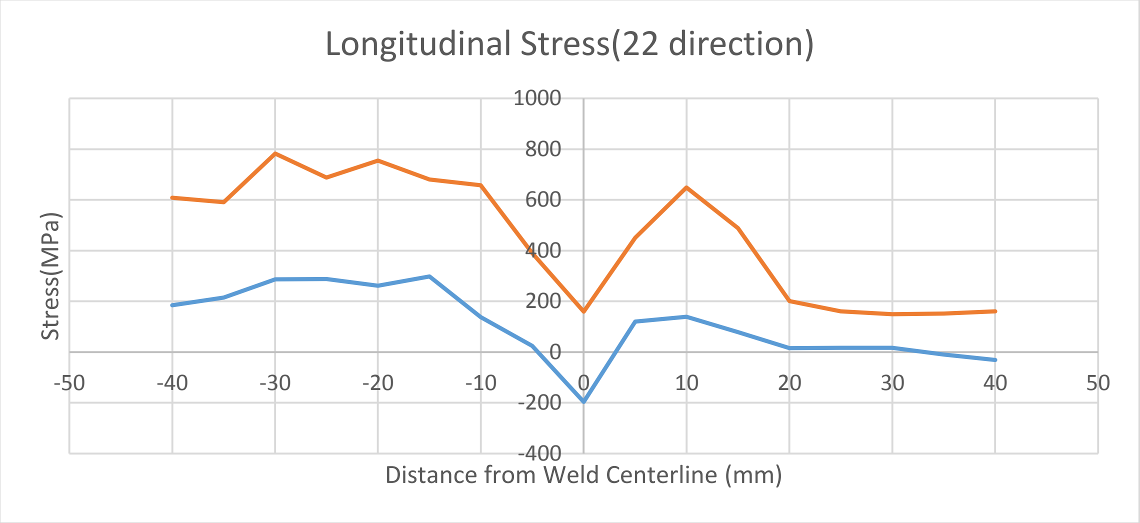

Figure 30. Longitudinal Stress Distribution across the Sample (orange line represents the triaxial state and blue line represents the biaxial state)

A more detailed calculation process could be find in Appendix A.

Discussion

Compare to Figure 31 which was included in a literature reference, both of the transverse stress data and longitudinal stress data measured were following the correct trend. [18] Both of them showed that there were large tensile stresses near the weld seam on each side of the weld. At the center of the weld, both longitudinal and transverse stress tended to be very small. On the other hand, the normal stress presented a completely different trend. It was very large at the center of the weld and became small when approaching to weld seams. Such trend confirmed with the one seen in the literature reference which is shown in Figure 32. [19] The trends of all three stress measurements were also found to be similar to the data obtained from neutron diffraction on the same material. Sample neutron diffraction data can be found in Appendix B. However, stress values obtained from X-ray diffraction were much higher than these from the neutron technique. This was due to the difference in penetration depth. We could only have a penetration depth of 22µm on 304 stainless steel by using X-ray while neutron could penetrate up to 15mm. Furthermore, according to Figure 33, the residual stress became larger as getting closer to the surface due to various machining processes, which perfectly explained the large stress values obtained by X-ray diffraction method. [20]

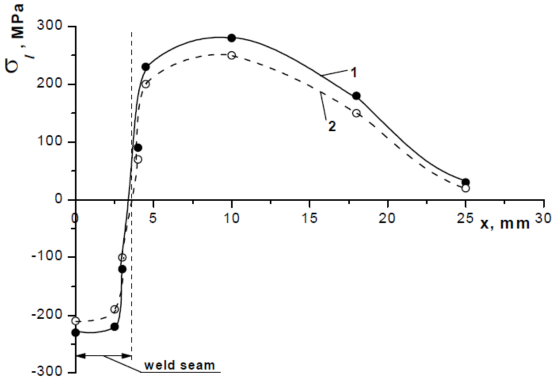

Figure 31. Residual Stress Distribution across the Sample: 1-longtudinal stress; 2-Transverse Stress [18]

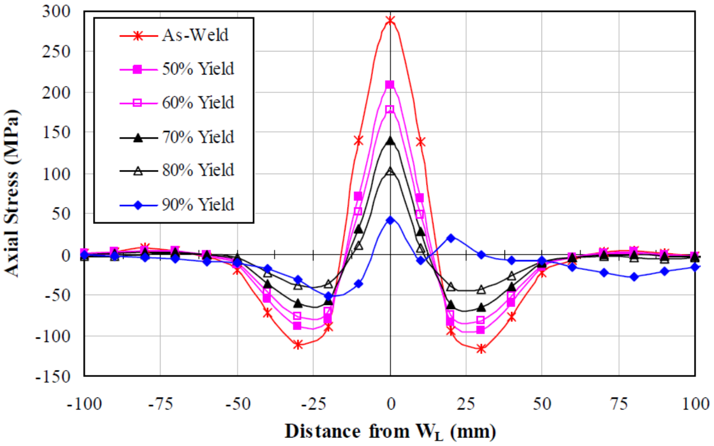

Figure 32. Normal Residual Stress Distribution in Welded Samples [19]

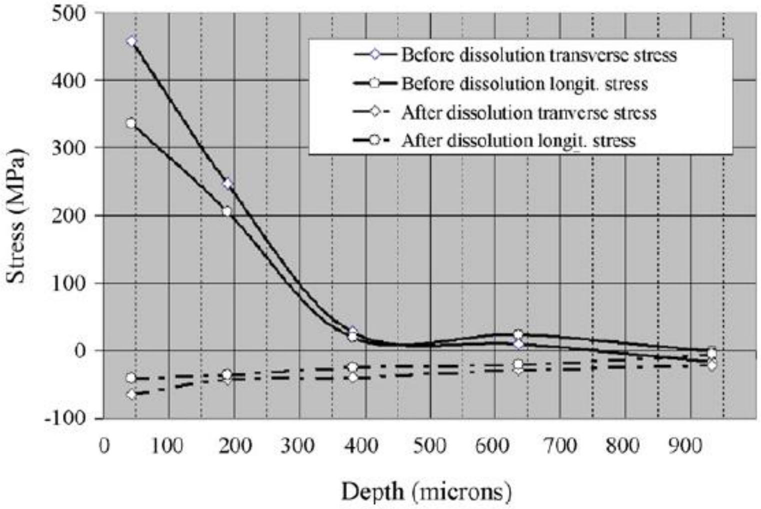

Figure 33. Surface Stress Distribution of As-machined Welded Sample [20]

When calculating transverse and longitudinal stresses, we looked into two cases: normal stress was zero and normal stress was nonzero. The stress values without the presence of normal stress were obtained through StressPlus software. Such software assumed the normal stress to be zero since the penetration depth was really small. Therefore, the software adopted the equations for calculating stress in a biaxial state automatically. However, according to the d_ψ vs. $\sin^2 \psi$ diagrams generated for each measurement point, there existed a split between measurements at positive and negative φ angle. Such information suggested that the normal stress could not be neglected. Since the software could not identify such situation, calculations were done by hand by using Eq.11 to Eq. 15. The stress values obtained with and without the presence of normal stress were compared in Figure 26, Figure 27, Figure 29, and Figure 30. From these figures, it could be concluded that normal stress had a huge influence to both transverse and longitudinal stress. It was important to have an accurate normal stress value so that the strain free d-spacing must be experimentally measured carefully. Data set one and data set two only used a slightly different d-spacing values but stress values showed more difference. Since d_0 used for data set two was taking from an annealed sample at its normalizing temperature, such value should be used for better accuracy.

There were various sources of error that might need to be consider. The first one was the misalignment of the instrument and the measuring samples. Detectors might misalign over usage time without causing any notice to the users so that it could affect the results obtained. During stress measurement, users were required to rotate the sample manually to different ϕ. Such rotation might contain minor errors which could also influence the results. Secondly, the sample’s surface might also cause errors in data. The samples being tested might not be flat throughout their entire surface and since stress measurement by X-ray diffraction was sensitive to sample’s height, errors might occur. Thirdly, the peak locations might not be identified accurately by the software due to small background noise. Lastly, the strain-free d-spacing value might not be the most accurate one due to cutting after annealing. Cutting might induce small residual stress to the sample which could result in distorted lattice parameter. [15]

Conclusion

The 304 stainless steel welded plates were susceptible to stress corrosion cracking through chlorine containing environment and residual stress due to welding. According to the phase diagram and microstructure figure, our samples possessed typical characteristics of 304 stainless steel. The hardness tests furthered confirmed that our samples were annealed after welding. From the stress measurements by using X-ray diffraction, we were able to see that at the weld seam on each side of the weld, there existed large tensile stresses in both transverse and longitudinal direction. At the center of the weld, stress values in both directions dropped sharply. The normal stress shared a completely different trend. It tended to be the maximum at the center of the weld and it became smaller while approaching the weld seam on each side. The stress trends in all three directions were confirmed by literature references and stress data obtained from neutron diffraction on the same material. However, the stress values measured by X-ray diffraction were large compared to the ones acquired from neutron method. This was due to the difference in penetration depth. X-ray diffraction could only had a penetration depth of 22 µm into the 304 stainless steel samples while neutron could have up to 15mm. The stress values near the surface tended to become very large due to various machining processes. There could be some sources of error such as instrument misalignment, rough sample surface, wrong peak searching in software, and inaccurate strain-free d-spacing values.

Bibliography

[1] R. Ballinger, "Life Prediction of Spent Fuel Storage Canister Material," U.S.Department of Energy, 2014.

[2] "United States Nulcear Regulation Commission," 20th October 2014. [Online]. Available: http://www.nrc.gov/waste/spent-fuel-storage/diagram-typical-dry-cask-system.html.

[3] "Nuclear Power Technology," 13th April 2014. [Online]. Available: http://criepi.denken.or.jp/en/activities/project/nuclear.html.

[4] R. Parrott and H. Pitts, "Chloride Stress Corrosion Cracking in Austenitic Stainless Steel," Health and Safety Executive, Derbyshire, 2011.

[5] G. Schajer and C. Ruud, "Overview of Residual Stresses and Their Measurement," in *Practical Residual Stress Measurement Methods*, Vancouver, WILEY, 2013, pp. 1-29.

[6] P. Cole, C. Ikeagu, A. Thistlethwaite, S. Williams, T. Nagy, W. Suder, A. Steuwer and T. Pirling, "The Welding Process Impact on Residual Stress and Distortion," *Science and Technology of Welding and Joining ,* pp. 717-725, 2009.

[7] "AK Steel," 3rd April 2014. [Online]. Available: http://www.aksteel.com/pdf/markets_products/stainless/austenitic/304_304L_Data_Sheet.pdf.

[8] S. Chosh and V. Kain, "Microstrutual Changes in AISI 304L Stainless Steel due to Surface Machining: Effect on its Susceptibility to Chloride Stress Corrosion Cracking," *Journal of Nulcear Materials ,* pp. 62-67, 2010.

[9] M. Prime and A. DeWald, "The Contour Method," in *Practical Residual Stress Measurement Methods*, Vancouver, WILEY, 2013, pp. 109-135.

[10] C. Murray and I. C. Noyan, "Applied and Residual Stress Determination Using X-ray Diffraction," in *Practical Residual Stress Measurement Methods*, Vancouver, University of British Columbia , 2013, pp. 139-161.

[11] T. Holden, "Neutron Diffraction," in *Practical Residual Stress Measurement Methods* , Vancouver, WILEY, 2013, pp. 195-221.

[12] G. Schajer and P. Whitehead, "Hole Drilling and Ring Coring," in *Practical Residual Stress Measurement Methods* , Vancouver, WILEY, 2013, pp. 29-61.

[13] M. Bateni, J. Szpunar, X. Wang and D. Li, "Wear and Corrosion Wear of Medium Carbon Steel and 304 Stainless Steel," *WEAR,* pp. 116-122, 2006.

[14] "ASTM Standards Info," 13th April 2015. [Online]. Available: http://astm.nufu.eu/std/ASTM+E2860+-+12.

[15] B. D. Cullity, Elements Of X Ray Diffraction, New Jersey: Prentice Hall , 2001.

[16] D. Ye, Y. Xu, L. Xiao and H. Cha, "Effects of Low-cycle Fatigue on Static Mechanical Properties, Microstructures, and Fracture Behavior of 304 Stainless Steel," *Materials Science & Engineering ,* pp. 4092-4102, 2010.

[17] "Lucideon," 20th April 2014. [Online]. Available: http://www.ceram.com/testing-analysis/techniques/x-ray-diffraction-xrd/rietveld-refinement/.

[18] J. Assis, V. Monin, J. Teodosio and T. Curova, "X-ray Analysis of Residual Stress Distribution in Weld Region," *Advances in X-ray Analysis,* pp. 225-231, 2002.

[19] "Mitigation of Weld Induced Residual Stresses by Mechanical Stress Relieving," *Pakistan Research Repository,* pp. 141-178.

[20] D. Thibault, P. Bocher and M. Thomas, "Residual Stress and Microstructure in Welds of 13%Cr–4%Ni Martensitic Stainless Steel," *Journal of Materials Processing Technology,* pp. 2195-2202, 2009.

[21] "Wasteland: the 50-year battle to entomb our toxic nuclear remains," 13th April 2014. [Online]. Available: http://www.theverge.com/2012/6/14/3038814/yucca-mountain-wipp-wasteland-battle-entomb-nuclear-waste.

Appendices

Appendix A Sample Data Calculation

The data used here is taking from the measurement at point 9 in set one.

Step 1. Export peak table from StressPlus software. This is done after accurately determining the peak locations in the software. Such table is shown as below.

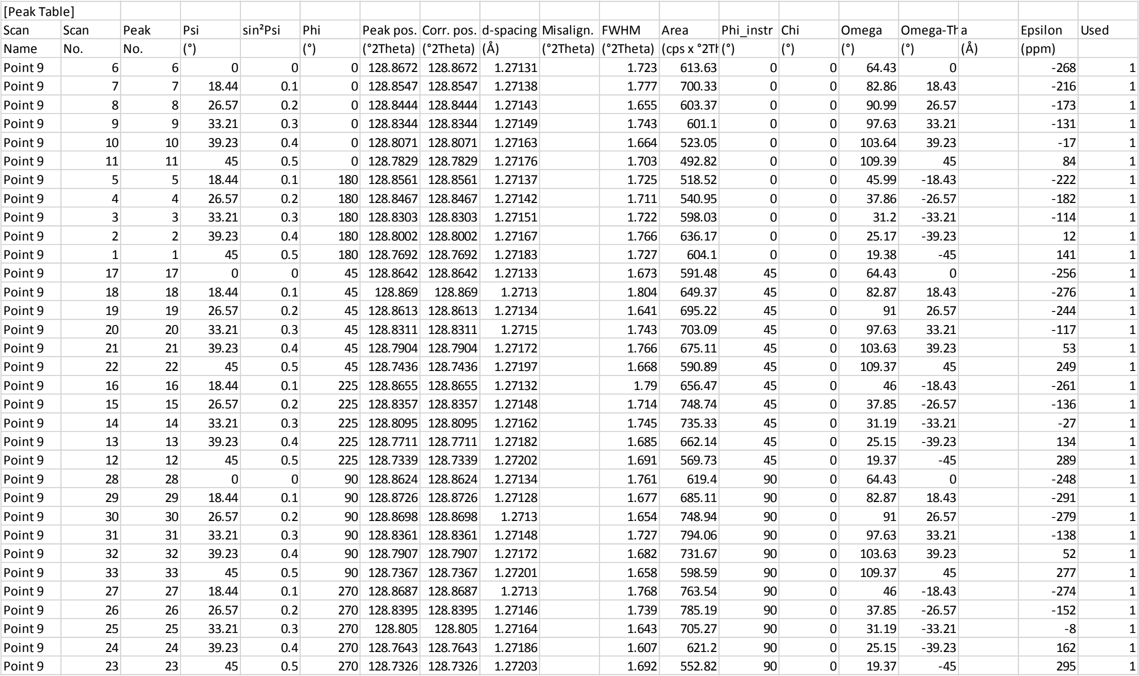

[Peak Table]																		
Scan Name	Scan No.	Peak No.	Psi (°)	sin^{2}Psi	Phi (°)	Peak pos. (°2Theta)	Corr. pos. (°2Theta)	d-spacing (Å)	Misalign. (°2Theta)	FWHM (°2Theta)	Area (cps x °2Tl	Phi_instr (°)	Chi (°)	Omega (°)	Omega-Tl (°)	a (Å)	Epsilon (ppm)	Used
Point 9	6	6	0	0	0	128.8672	128.8672	1.27131		1.723	613.63	0	0	64.43	0		-268	1
Point 9	7	7	18.44	0.1	0	128.8547	128.8547	1.27138		1.777	700.33	0	0	82.86	18.43		-216	1
Point 9	8	8	26.57	0.2	0	128.8444	128.8444	1.27143		1.655	603.37	0	0	90.99	26.57		-173	1
Point 9	9	9	33.21	0.3	0	128.8344	128.8344	1.27149		1.743	601.1	0	0	97.63	33.21		-131	1
Point 9	10	10	39.23	0.4	0	128.8071	128.8071	1.27163		1.664	523.05	0	0	103.64	39.23		-17	1
Point 9	11	11	45	0.5	0	128.7829	128.7829	1.27176		1.703	492.82	0	0	109.39	45		84	1
Point 9	5	5	18.44	0.1	180	128.8561	128.8561	1.27137		1.725	518.52	0	0	45.99	-18.43		-222	1
Point 9	4	4	26.57	0.2	180	128.8467	128.8467	1.27142		1.711	540.95	0	0	37.86	-26.57		-182	1
Point 9	3	3	33.21	0.3	180	128.8303	128.8303	1.27151		1.722	598.03	0	0	31.2	-33.21		-114	1
Point 9	2	2	39.23	0.4	180	128.8002	128.8002	1.27167		1.766	636.17	0	0	25.17	-39.23		12	1
Point 9	1	1	45	0.5	180	128.7692	128.7692	1.27183		1.727	604.1	0	0	19.38	-45		141	1
Point 9	17	17	0	0	45	128.8642	128.8642	1.27133		1.673	591.48	45	0	64.43	0		-256	1
Point 9	18	18	18.44	0.1	45	128.869	128.869	1.2713		1.804	649.37	45	0	82.87	18.43		-276	1
Point 9	19	19	26.57	0.2	45	128.8613	128.8613	1.27134		1.641	695.22	45	0	91	26.57		-244	1
Point 9	20	20	33.21	0.3	45	128.8311	128.8311	1.2715		1.743	703.09	45	0	97.63	33.21		-117	1
Point 9	21	21	39.23	0.4	45	128.7904	128.7904	1.27172		1.766	675.11	45	0	103.63	39.23		53	1
Point 9	22	22	45	0.5	45	128.7436	128.7436	1.27197		1.668	590.89	45	0	109.37	45		249	1
Point 9	16	16	18.44	0.1	225	128.8655	128.8655	1.27132		1.79	656.47	45	0	46	-18.43		-261	1
Point 9	15	15	26.57	0.2	225	128.8357	128.8357	1.27148		1.714	748.74	45	0	37.85	-26.57		-136	1
Point 9	14	14	33.21	0.3	225	128.8095	128.8095	1.27162		1.745	735.33	45	0	31.19	-33.21		-27	1
Point 9	13	13	39.23	0.4	225	128.7711	128.7711	1.27182		1.685	662.14	45	0	25.15	-39.23		134	1
Point 9	12	12	45	0.5	225	128.7339	128.7339	1.27202		1.691	569.73	45	0	19.37	-45		289	1
Point 9	28	28	0	0	90	128.8624	128.8624	1.27134		1.761	619.4	90	0	64.43	0		-248	1
Point 9	29	29	18.44	0.1	90	128.8726	128.8726	1.27128		1.677	685.11	90	0	82.87	18.43		-291	1
Point 9	30	30	26.57	0.2	90	128.8698	128.8698	1.2713		1.654	748.94	90	0	91	26.57		-279	1
Point 9	31	31	33.21	0.3	90	128.8361	128.8361	1.27148		1.727	794.06	90	0	97.63	33.21		-138	1
Point 9	32	32	39.23	0.4	90	128.7907	128.7907	1.27172		1.682	731.67	90	0	103.63	39.23		52	1
Point 9	33	33	45	0.5	90	128.7367	128.7367	1.27201		1.658	598.59	90	0	109.37	45		277	1
Point 9	27	27	18.44	0.1	270	128.8687	128.8687	1.2713		1.768	763.54	90	0	46	-18.43		-274	1
Point 9	26	26	26.57	0.2	270	128.8395	128.8395	1.27146		1.739	785.19	90	0	37.85	-26.57		-152	1
Point 9	25	25	33.21	0.3	270	128.805	128.805	1.27164		1.643	705.27	90	0	31.19	-33.21		-8	1
Point 9	24	24	39.23	0.4	270	128.7643	128.7643	1.27186		1.607	621.2	90	0	25.15	-39.23		162	1
Point 9	23	23	45	0.5	270	128.7326	128.7326	1.27203		1.692	552.82	90	0	19.37	-45		295	1

Step 2. Use d-spacing values at (φ=0,ϕ=0), (φ=0,ϕ=45), and (φ=0,ϕ=90) to determine normal strain in 33 direction by using Eq. 15. All three d-spacing values should be the same. If they are slightly different, an average value can be used. Table below shows an example.

ϕ Value	D-spacing Value
ϕ=0	1.27131
ϕ=45	1.27133
ϕ=90	1.27134
Average	1.271327

Step 3. Apply Eq.11 to Eq. 15 to calculate strain in six directions. This should be done at (ϕ=0,180), (ϕ=90,270) and if interested, (ϕ=45,235). A sample calculation is listed below calculating at ϕ=0,180.

Sin^2 φ	d1	d2	a1
0	1.27131	1.27131	-0.00046
0.1	1.27138	1.27137	-0.0004
0.2	1.27143	1.27142	-0.00037
0.3	1.27149	1.27151	-0.00031
0.4	1.27163	1.27167	-0.00019
0.5	1.27176	1.27183	-7.5E-05

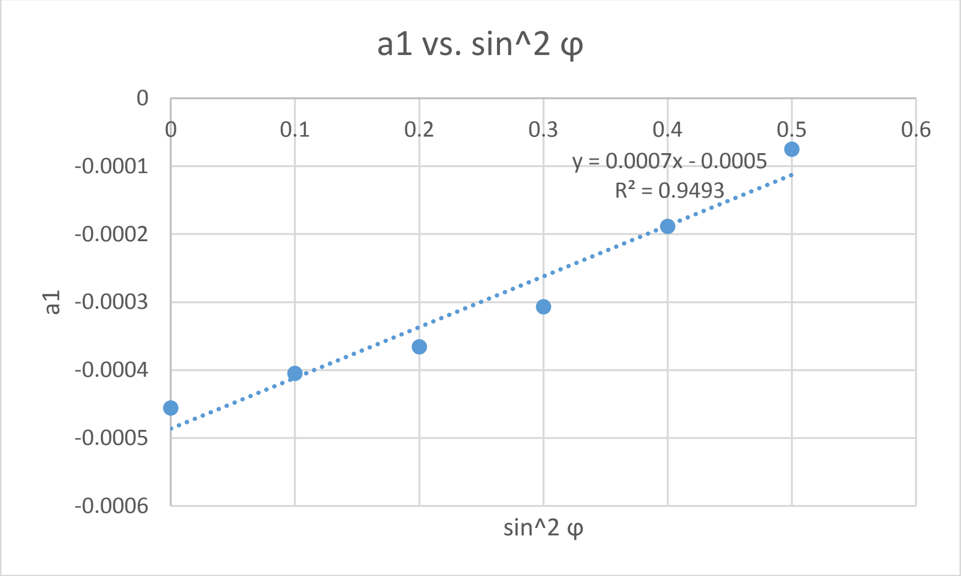

Step 4. Applied the slope of a1 vs. sin^2 φ and normal strain into Eq. 12 to get strain in interested direction. The stress value can be calculated by multiplying the strain with elastic modulus and one plus Poisson's ratio.

Appendix B Sample Neutron Diffraction Data

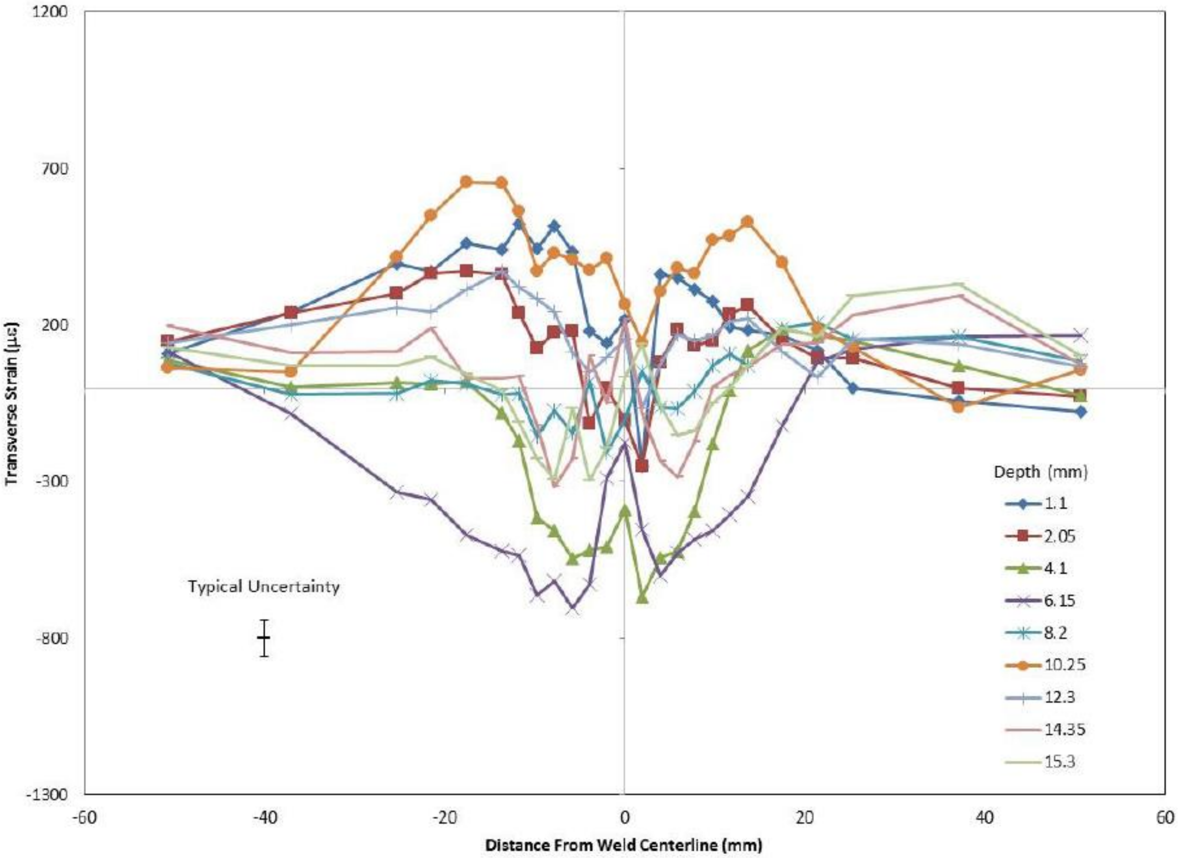

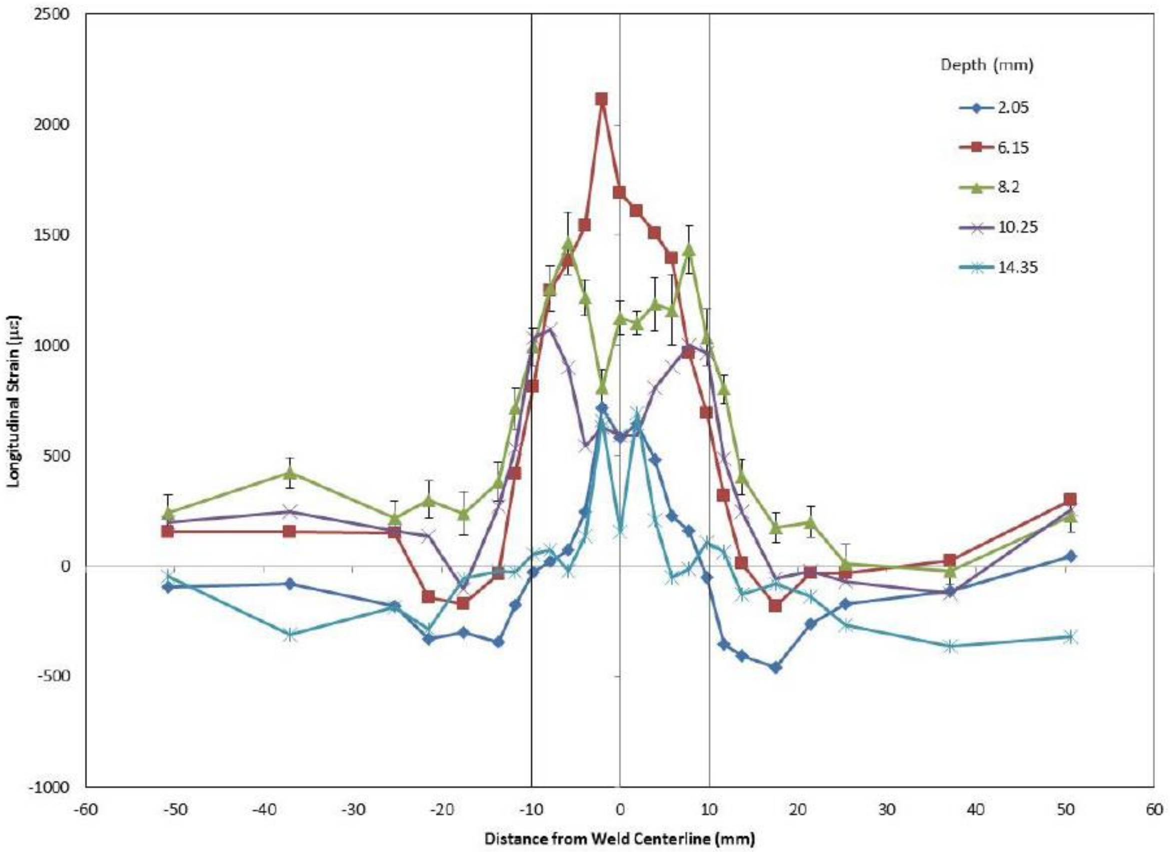
Depth (mm)
2.05
6.15
8.2
10.25
14.35
Longitudinal Strain (με)
Distance from Weld Centerline (mm)
2500
2000
1500
1000
500
0
-500
-1000
-60
-50
-40
-30
-20
-10
0
10
20
30
40
50
60

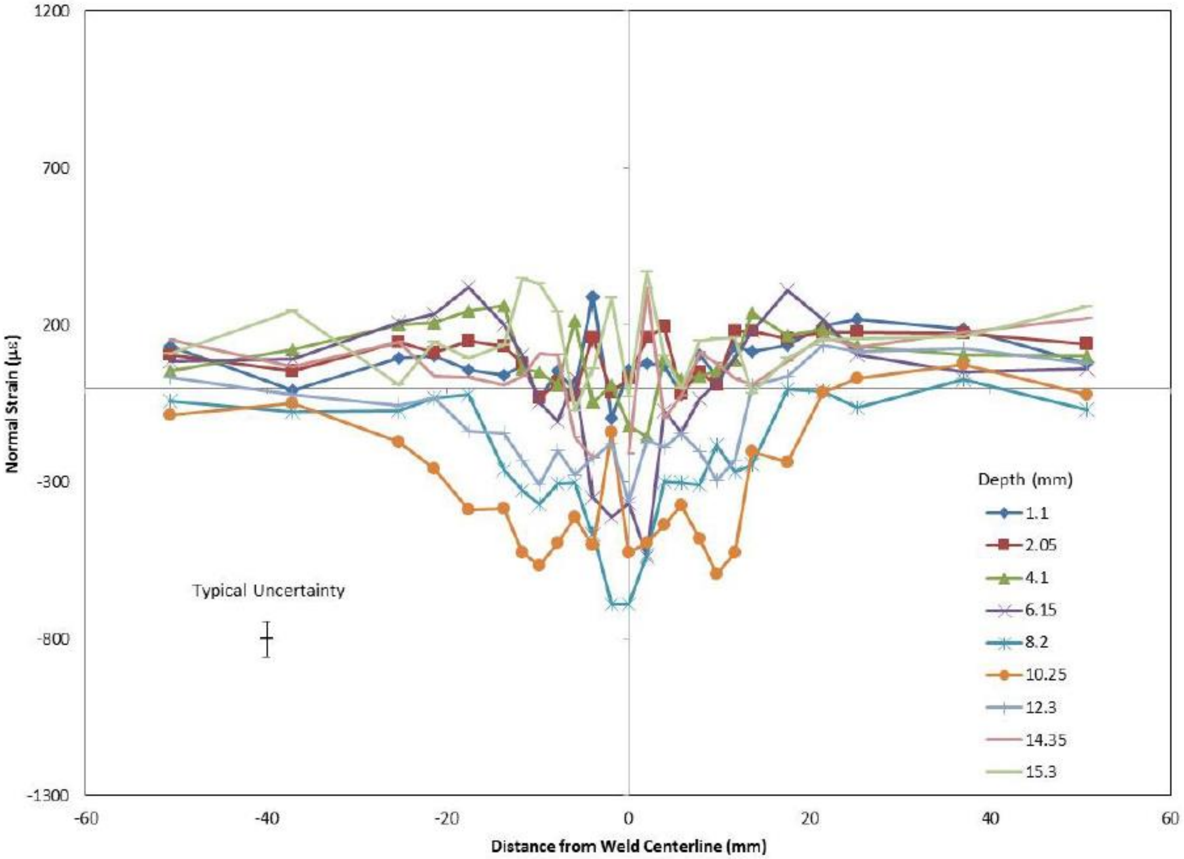
1200
700
200
-300
-800
-1300
Normal Strain (µε)
-60
-40
-20
0
20
40
60
Distance from Weld Centerline (mm)
Typical Uncertainty
Depth (mm)
1.1
2.05
4.1
6.15
8.2
10.25
12.3
14.35
15.3